

Abstract

Walter, Jennifer Jean Huening. Raman Scattering Analysis of Structural Transformations Due to Precision Engineered Si, 6H-SiC and β -Si₃N₄. (Under the direction of Robert J. Nemanich)

This thesis explores the local residual structural transformations that result from indentation and ductile material removal of machined Si, 6H-SiC, and β -Si₃N₄. During the machining process, very high pressures can be achieved at the contact interface between the machining tool and the surface of a material. The induced pressures can cause transformations through a series of phases, and upon releasing the pressure, the material can again be transformed to a new phase. Many of the high-pressure phases of Si, and some of the phases of SiC and β -Si₃N₄ have been defined experimentally for hydrostatic pressure conditions in diamond anvil cell experiments, and have also been predicted theoretically. However, the complexity of plastic deformation complicates the transition process from non-hydrostatic pressure causes the response of the material to be difficult to define for precision engineered and machined surfaces. In these cases, the transmission of applied force can be dependent on nonhydrostatic structural changes due to plastic flow, and structural transitions can be induced at lower pressures than would occur, if at all, for hydrostatic pressures. The Raman technique is employed as a nondestructive structure sensitive probe to investigate the structural and vibrational properties of indented and machined Si, 6H-SiC, β -Si₃N₄. Visible Raman scattering of Si indentations indicate that localized regions are transformed into metastable phases. On machined Si surfaces, a layer of amorphous material is observed, and the depth of this

layer has been found to be dependent on the machining conditions. For the wide bandgap materials, 6H-SiC and β -Si₃N₄, the short absorption depth of UV light allows for accurate probing of the surface, and the transparency to visible light allows analysis of the bulk material. The studies on indentations made on the 6H-SiC (0001) surface indicate biaxial stress from point pressure. Machined 6H-SiC basal plane edges of (0001) wafers indicate that the near surface structure is changed from single crystal to polycrystalline. Studies conducted on nm and μ m precision-machined β -Si₃N₄ reveals transformation of a surface layer into an amorphous phase. Probing the depth dependence through wavelength selection provides information on the depth of the amorphous zone. In addition, the chips that are produced during machining are found to transform to an amorphous phase.

**Raman Scattering Analysis of Structural Transformations Due to Precision
Engineered Si, 6H-SiC and β -Si₃N₄**

by

Jennifer Jean Huening Walter

A thesis submitted to the Graduate Faculty of
North Carolina State University
in partial fulfillment of the
requirements for the Degree of
Master of Science

Department of Physics

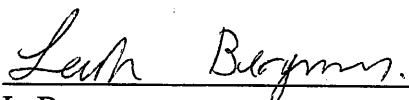
Raleigh

November 1, 2004

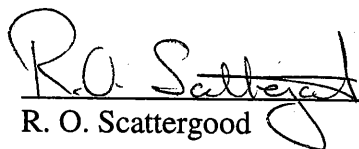
Approved by:



H.D. Hallen



L. Bergman



R. O. Scattergood



R.J. Nemanich
Chair of Advisory Committee

Dedication

To my parents, Linda and Peter Huening.

Biography

Jennifer Walter was born July 24, 1980 in Longbranch, New Jersey. She and her parents moved to New York State in 1984 and back to New Jersey in 1992. Jennifer graduated from Jackson memorial high school, NJ, in 1999, with a strong desire to pursue a career in science. She attended The College of New Jersey for her first two years of college. Her studies were directed toward a degree in Physics with a computer science concentration. In the summer of 2001, she did a research for undergraduates experience (REU) in astrophysics at North Carolina State University under the direction of Professor Reynolds before transferring to the school to finish her degree in Physics. In the summer of 2002, Jennifer did a different REU with the surface science lab (SSL) at North Carolina State University under the direction of Professor Nemanich. She joined the SSL group for the school year, and in May 2003, received a B.S. degree in Physics. After graduating, Jennifer continued doing research with the SSL group for graduate studies. In the summer of 2003, she did an internship at Intel Corporation in Hillsboro, OR. On August 21, 2004 she married her husband, David Walter. Jennifer expects to finish her M.S. in physics at North Carolina State University in December 2004.

Acknowledgements

The author would like to greatly acknowledge the support and guidance of the faculty, students, and staff of the Department of Physics. I would also like to thank the high-pressure phase transformation group, Jae-il Jang, Songqing Wen, George Pharr, John Patten, Lei Dong, Jimmie Miller, Travis Randall, and Ronald Scattergood, for their contributions to the work, fruitful discussions, and for the opportunity to take part in this research project. I would like to thank the SSL group, both past and present, Lena Fitting, Billyde Brown, Dr. Minseo Park, Anderson Sunda-Meya, Dr. Brian Coppa, Dr. Ted Cook, Dr. Jaesob Lee, Mengning Liang, Charlie Fulton, James Burnette, Joe Tedesco, Matt Zeman, Jacob Garguilo, Franz Koeck, Yunyu Wang, Will Mecouch, Dr. Woochul Yang, Eugene Bryan, and Tom Blair, for their help in experiments and analyzing results, in addition to their friendships. I would like to thank our administrative assistants, C.J. Hathorne and Cecilia Upchurch, for always taking care of the SSL group.

I am grateful to my committee members, Ronald Scattergood, Hans Hallen, and Leah Bergman, who have all played a significant role in my education through classes and/or research. I'd like to give special thanks to my advisor, Robert J. Nemanich, for the opportunities and freedom he has given me throughout this research, in addition to, his support, intellectual insight, and guidance.

Lastly, I'd like to thank my sister, Jessica Huening, my parents, Linda and Peter Huening, and my husband, David Walter, for their unconditional encouragement and support throughout all of my life experiences.

Table of Contents

List of Figures	vii
List of Tables.....	xi
Ch. 1: Introduction.....	1
1.1: References.....	4
Ch. 2: Raman Scattering Analysis of Si, SiC and Si ₃ N ₄	5
2.1: Origin of the Raman scattering spectrum.....	5
2.2: Raman scattering modes of Si, 6H-SiC and β-Si ₃ N ₄	6
2.3: Raman scattering analysis of material structures.....	8
2.4: Stress Measurements of Raman scattering modes.....	10
2.5: Probing depth dependence on incident wavelength.....	12
2.6: References.....	13
Ch. 3: Transformations in Si, SiC and Si ₃ N ₄	21
3.1: Transformation Process.....	22
3.2: Transformations in Si.....	23
3.3: Transformations in SiC.....	24
3.4: Transformations in Si ₃ N ₄	24
3.5: References.....	26
Ch. 4: Raman Scattering Analysis of Indented and Machined Si.....	29
4.1: Experiment summary.....	29
4.2: Experimental details.....	30
4.3: Results.....	31
4.4: Discussion.....	34

4.5: Conclusions.....	36
4.6: References.....	37
Ch. 5: UV Raman Scattering Analysis of Indented and Machined 6H-SiC.....	46
5.1: Experiment summary.....	46
5.2: Experimental details.....	46
5.3: Results.....	48
5.4: Discussion.....	53
5.5: Conclusions.....	55
5.6: References.....	57
Ch. 6: UV Raman Scattering Analysis of Machined β -Si ₃ N ₄	69
6.1: Experiment summary.....	69
6.2: Experimental details.....	69
6.3: Results.....	70
6.4: Discussion.....	72
6.5: Conclusions.....	81
6.6: References.....	82
Ch. 7: Concluding Remarks and Future Directions.....	79

List of Figures

2.1	The phonon dispersion curve for 6H-SiC in the large zone.....	14
2.2	Micro Raman scattering of Si chips showing the crystalline Si peak at 520Rcm^{-1} and a heated peak at lower relative wavenumbers. The spectra (a) to (d) are from lower to higher power, respectively.....	17
2.3	The peak position of the Raman scattering spectra from Si chips versus laser power. The vertical scale on the right represents the temperature that would correspond to the observed Raman scattering peak shift.....	18
2.4	Decay of the Raman scattering signal with depth in the sample for (a) single crystal Si (b) single crystal 6H-SiC and (c) $\beta\text{-Si}_3\text{N}_4$. The probing depth is defined as the depth where the intensity is 37% of the incident.....	19
3.1	Micro Raman scattering spectra of three SiC wafers which show the dominant TO modes at $\sim 760\text{Rcm}^{-1}$ and the LO modes at $\sim 970\text{Rcm}^{-1}$ for (a) 4H-SiC, (b) 6H-SiC, and (c) a mixture of 4H and 6H SiC.....	28
4.1	One-step load displacement curves for (a) 100 and (b) 200 mN maximum load indents. An indentation rate of 5 mN/s was employed.....	38
4.2	SEM images of Si indentations for maximum loads of (a) 100, (b) 200, and (c) 700 mN. An indentation rate of 5 mN/s was employed.....	39
4.3	Micro Raman scattering spectra taken from the center of a Si indentation obtained with a maximum load (a) 100, (b) 200, and (c) 700 mN.....	40
4.4	Schematic of the typical damage pattern observed from machined (001) and (111) surfaces of a diamond cubic lattice.....	41

4.5	Macro Raman scattering spectra of machined Si (111) wafer machined in the $[1\bar{1}0]$ direction with a rake angle of -45° and with a feed rate of (a) 5 and (b) 1 $\mu\text{m}/\text{rev}$	42
4.6	Macro Raman scattering spectra of machined Si (001) surfaces for rates varying from (a) 15 (b) 7 (c) 3 (d) 2 to (e) 1 $\mu\text{m}/\text{rev}$. The surfaces were machined in the $[010]$ direction.....	43
4.7	Macro Raman scattering spectra of machined Si (111) surfaces with a rake angle of (a) -25° and (b) -45° . The machining rate was 1 $\mu\text{m}/\text{rev}$., and the direction of cut was along $[110]$	44
4.8	Macro Raman scattering spectra of a machined Si (111) wafer with a rake angle of -45° and feed rate 1 $\mu\text{m}/\text{rev}$. for ductile machining wafer directions of (a) $[1\bar{1}0]$, (b) $[\bar{1}\bar{1}2]$, and (c) $[11\bar{2}]$	45
5.1	Schematic (a) of the machining process and (b) 6 fold symmetry directions of 6H-SiC (0001) wafer.....	58
5.2	The load displacement curve for indentation of a 6H-SiC(0001) surface with a maximum load of 200 mN.....	59
5.3	An SEM image of the surface of indented 6H-SiC. A maximum load of 200 mN was used.....	60
5.4	UV micro Raman scattering spectra display the TO and LO modes for (a) center of the indent (b) edge of the indent (c) surrounding area (d) reference area for indentation with a maximum load of 200 mN.....	61
5.5	The local stress (in units of pressure) in regions in and surrounding an indent. The values were deduced from the transverse (TO) and longitudinal (LO) Raman	

	scattering modes. The results were obtained from indents produced from a maximum indentation load of 200mN, and the stress was deduced using the relations from Liu, et al.....	62
5.6	Polar plot of the cutting force dependence on the 6-fold symmetry of 6H-SiC machined wafer edges. The plot was obtained for a rake angle of 0°, and a cutting depth of 100 nm.....	63
5.7	Optical image of ductile chip removal. A rake angle of -45°, and a depth of cut of 500 nm were employed.....	64
5.8	UV macro Raman scattering spectrum of (a) machined 6H-SiC edge and (b) polished wafer. For comparison, the (c) calculated vibrational density of states (DOS) of SiC is presented.....	65
5.9	UV micro Raman scattering spectra of machined 6H-SiC edges for rake angles of (a) -45°, (b) -30°, and (c) 0°. The spectra were obtained with incident light along the $[11\bar{2}0]$ direction of the wafer.....	66
5.10	UV macro Raman scattering spectra of machined 6H-SiC edges for machining depths of (a) 50, (b) 250, and (c) 500 nm depth of cut per revolution. The spectra were obtained with the incident light along the $[11\bar{2}0]$ direction of the wafer.....	67
5.11	UV micro Raman scattering spectra of a (a) dark spot on the machined surface (b) compared to the machined surface of a 6H SiC wafer.....	68
6.1	SEM image (400 μm x 400 μm) of debris from machined $\beta\text{-Si}_3\text{N}_4$	75
6.2	UV Raman scattering spectra of (a) grounded and machined (b) 5 μm (c) 10 μm and (d) 500 nm polycrystalline $\beta\text{-Si}_3\text{N}_4$	76

- 6.3 (a) Macro Raman scattering spectrum of the bulk of machined β -Si₃N₄ is shown for 514.5 nm. Micro Raman scattering spectra with (b) 325 and (c) 244 nm incident wavelengths.....77
- 6.4 (a) Macro and (b) micro Raman scattering spectrum of the chips removed during the machining process for a 5 μ m depth of cut.....78

List of Tables

- 2.1 The vibrational frequencies are given for (a) propagation angles relative to the c -axis and (b) the weaker modes are valid for any propagation direction and are assigned to values of $x = q / q_{\max}$ in the large zone. All values are experimental except the figures in parenthesis, which are calculated.....15
- 2.2 Backscattering first-order Raman scattering active modes of β -Si₃N₄ in Rcm⁻¹.....16
- 2.3 Calculated probing depths for single crystal Si, single crystal 6H-SiC, and β -Si₃N₄. The probing depth is defined as the depth where the intensity is 37% of the incident intensity.....20

1. Introduction

As technology advances lead to the development of higher precision products, a demand to understand the structural properties of precision engineered materials on a μm and nm scale is required. The knowledge could be used to enhance macroscopic properties through, for example, patterning of nano scale phases with unique electrical, mechanical, or optical characteristics or optimization of micromachined wafer surfaces by establishing machining parameters that will increase ductility. A scientific basis for these practices can be established from investigation and characterization of structural changes in the materials. The processes in which one structure transforms to another have yet to be fully understood. For instance, there are over 200 polytypes identified in SiC ,¹ but little work has been done to understand the transformations between them. This thesis is devoted to the identification of structural changes on the surfaces of precision engineered and machined single crystal Si, single crystal 6H-SiC, and polycrystalline $\beta\text{-Si}_3\text{N}_4$. Raman spectroscopy is used as the main characterization tool providing evidence of local bonding structure through analysis of the vibrational properties of the processed indented and machined surfaces. Particular emphasis is given to transformation to metastable and polycrystalline or amorphous structures, which can result from densification and relaxation of the material generated by the high pressures that are achieved at the contact interface between the machining tool and the material. A significant portion of this thesis is devoted to interpretation of the Raman spectra from indented and machined surfaces.

The materials chosen for study are brittle, but they have the potential to undergo transformation with the application of high pressures. Si has been widely studied and structural transformations resulting from the application of high-pressures have been characterized by several researchers.² Of particular interest is the ductility of this material, which is thought to derive from a complex series of transformations during the machining process. Diamond anvil cell experiments have confirmed that under high nearly hydrostatic pressures (~13 GPa) Si will be transformed to a metallic β -Sn phase³ and has been reported to relax to either a metastable Si III phase³ or an amorphous phase depending on the rate in which the pressure was applied. The same residual metastable and amorphous phases have been detected on the surfaces of precision-engineered materials providing evidence that the β -Sn phase is attainable from localized pressures, which consequently result in plastic flow. Additional diamond anvil cell experiments have reported a decrease in the onset of the transition pressure to the metallic phase from ~11.3 GPa for hydrostatic stresses to ~8.5 GPa for uniaxial stress.⁴ These measurements indicate that the nonhydrostatic component of stress plays a role in the transformation process. The observed ductility of the material may be directly related to the extent of the residual phases after machining. The phenomenon observed in the investigations on Si is now being expanded to the ceramic semiconductors, 6H-SiC and β -Si₃N₄.

In this thesis, visible and UV Raman spectroscopy are used as the main characterization tools to investigate the structural changes on the surfaces of indented and machined materials. Raman spectroscopy is a non-destructive technique that requires little or no specimen preparation. With focusing optics, specific collection areas on the order of μm

can be sampled. Visible Raman spectroscopy can be applied to Si, however, for the wide bandgap materials of 6H-SiC and β -Si₃N₄, visible light penetrates throughout the material, and UV light must be used to analyze the surfaces. The surface layer thickness affected by the external mechanical forces range from nm to μm . A probing depth less than 35 nm for SiC and less than 1.4 μm for Si₃N₄ can be achieved with UV excitation. The Raman technique is valuable because each structure displays an identifiable Raman signature. A change in structure may affect the position, line width, line shape, and intensity of the Raman signal. Moreover, the observation of new, and clearly identifiable peaks can be associated with the presence of different phases.

1.1 References

1. A. Addamiano, in *Silicon Carbide-1973*, edited by R.C. Marshall, J. W. Faust, Jr. and C.E. Ryan, University of South Carolina, Columbia 179, (1974).
2. Domnich, V., Gogotsi, Y., *Exper. Methods in the Phys. Sciences* 38, 355 (2001).
3. H. Olijnyk, S.K. Sikka, and W.B. Holzapfel, *Phys. Lett. A* 103, 137 (1984).
4. J.Z. Hu, L.D. Merkle, C.S. Menoni, I.L. Spain, *Phys. Rev. B* 34, 4679 (1986).

2. Raman Scattering Analysis of Si, SiC and Si₃N₄

2.1 Origin of the Raman scattering spectrum

The vibrational spectrum of a solid can be described by a frequency distribution (*i.e.* density of states) or a set phonon dispersion curves, which relate the frequencies and wavevectors of each of the allowed modes. Momentum conservation requires that only phonons that have a projection onto the incident and scattered light fields will scatter light. Therefore, since light exhibits a wavevector $k \approx 1/1000$ of the Brillouin zone boundary wavevector, Raman scattering measures $k \approx 0$ phonons. The phonons at the zone center are dependent on the number of atoms in the unit cell. They are comprised of acoustic phonons, in which the atoms in each unit cell vibrate in phase with one another, and optic phonons, in which the atoms in the unit vibrate with respect to one another. There are 3 acoustic vibrations and $3(n-1)$ optic vibrations, where n is the number of atoms in the unit cell. The frequencies of vibration depend on the bonding of the atoms within the unit cell.

The scattering efficiency depends on the polarization of the incident and scattered lights and is given by

$$I = C \sum_j |e_i \cdot R_j \cdot e_s|^2 \quad (2.1)$$

Here, C is a constant, R is the Raman tensor of phonon j , and e_i and e_s are the polarization vectors of the incident and scattered light, respectively. For a complete review of the scattering efficiency in crystals, Loudon has derived the Raman tensors for

the 32-crystal classes.¹ All Raman measurements presented in this thesis are the Stokes shifted spectra. The notation, Rcm^{-1} , represents the wavenumber shift of the observed mode from the incident laser frequency.

2.2: Raman scattering modes of Si, 6H-SiC and β -Si₃N₄

A. Raman scattering modes of Silicon

The structure of Si in its stable form is diamond cubic and is of the space group $Fd3m$ O^7_h . The first order Raman spectrum of crystalline Si at room temperature has a triply degenerate peak at 520 relative wavenumbers with a full-width at half maximum (FWHM) of 3.122cm^{-1} . The Raman spectrum of amorphous Si has two main bands at 150 Rcm^{-1} and 480 Rcm^{-1} , which are commonly assigned as transverse acoustic (TA) and transverse optic (TO) bands.² It has been found that the TA/TO intensity ratio and the TO linewidth increases with increasing degree of structural disorder.³

B. Raman scattering modes of 6H-Silicon Carbide

The crystal structure of 6H-SiC is uniaxial with a hexagonal structure and 6-fold symmetry. 6H-SiC is of the space group C^4_{6v} . The zone center normal modes are given by the irreducible representation $\Gamma = 6(A_1 + B_1 + E_1 + E_2)$ where the $5A_1$, $5E_1$, and $6E_2$ modes are Raman active, and the A_1 and E_1 modes are also infrared active. There are 12 atoms per unit cell, and therefore, 33 optic phonons and 3 acoustic phonons. The modes in which the Si and C sublattices vibrate against each other include the transverse optic TO modes (vibrations perpendicular to the c -axis) with E_1 and $(A_1 + E_1)$ symmetry and the longitudinal optic LO mode (vibrations parallel to the c -axis) with $(A_1 + E_1)$

symmetry.⁴ In the 180° backscattering geometry, the symmetry becomes E_1 and A_1 for the TO modes and E_1 for the LO mode. Additional weaker modes are observed for 6H-SiC. The symmetries of these modes and the modes of the various polytypes of SiC have been previously assigned.^{5,6} The phonon dispersion curve for 6H-SiC is provided in Fig. 1 and is represented in the large zone scheme extending to $6\pi/a$ where a is the lattice constant of a unit cell. Since $2\pi/a$ is a reciprocal lattice vector, the pseudomomentum vectors $q=0$, $q=2\pi/a$, $q=4\pi/a$, $q=6\pi/a$ are all equivalent to the $q=0$ point in the Brillouin zone. The corresponding frequencies and symmetries are listed in Table 1, where it is assumed that the incident laser propagates parallel to the c -axis. The broadened phonon density of states of amorphous SiC has broadband features in the range of 650 Rcm^{-1} to 1700 Rcm^{-1} .⁷

C. Raman scattering modes of β - Silicon Nitride

The β -Si₃N₄ crystals are hexagonal in structure and belong to the space group $C_{6h}^2(P6_3/m)$. The irreducible representation for the β -Si₃N₄ zone center phonons is given by $\Gamma_{optic} = 4A_g + 2A_u + 3B_g + 4B_u + 2E_1 + 5E_{2g} + 4E_{1u} + 2E_{2u}$, and $\Gamma_{acoustic} = A_u + E_{1u}$. The Raman active modes are the $4A_g$, $2E_{1g}$, and E_{2g} , where the $2E_{1g}$, and E_{2g} modes are doubly degenerate. The A_u and E_{1u} modes are infrared active. The Raman frequencies and symmetries for β -Si₃N₄ are provided in Table 2. For polycrystalline materials the signal represents an average of all grain orientations, and the propagation direction, is therefore, not significant. The vibrational density of states of amorphous Si₃N₄ contains two very broadened peaks centered at about 400 Rcm^{-1} and 900 Rcm^{-1} .⁸

2.3: Raman scattering analysis of material structures

The Raman scattering matrix element will affect the relative intensity of the sharp modes from crystalline materials and the broad bands of amorphous materials. In addition to stress effects, careful attention must be given to discerning between polycrystalline, nanocrystalline, amorphous, and highly dislocated material. Moreover, a distinction between the Raman spectrum of the various structures and heated material should be made when using high power densities in micro Raman experiments.

The Raman spectrum for finite crystal domains has been previously explained with a phonon confinement model.^{9, 10} The wavevector of the vibrational excitation is uncertain by a factor of $\Delta k = 2\pi / L$, where L is the crystal dimension, and therefore, the wavevector selection rules for Raman scattering from a finite sized crystal will be uncertain to this degree. Considering that the Brillouin zone boundary is π / a , where a is the lattice constant, this effect becomes significant in the Raman spectrum when crystal domains are less than 100 nm. Based on this model and experimental observations, relaxation of the k -vector selection rules will cause the full width at half maximum (FWHM) of the Raman peaks to increase with decreased grain size. A shift in frequency can also occur. In the limit where the domain size decreases to zero and the structure resembles a random network, the material is amorphous, all of the Raman modes become active, and the spectrum resembles the density of states.

In amorphous materials, due to the loss of long-range order, all of the vibrational modes have a component that satisfies the wavelength matching conditions of the incident and

scattered light. Therefore, the spectra will often resemble the broadened density of states. The relative intensity of specific bands is also enhanced or suppressed depending on the Raman matrix element.

A Raman spectrum of a crystal is dependent on the long-range order, and therefore, a small number of dislocations may not be detected. However, highly dislocated material will decrease the Raman phonon lifetime leading to peak broadening. For very high dislocation densities the phonon scattering length will be significantly resemble amorphous material.

The temperature of a material can affect the Raman modes due to volume expansion and higher order anharmonic interactions. As temperature is decreased, an increase in the intensity ratio between the Stokes and anti-Stokes lines is observed because there are fewer vibrational states initially in the excited state as temperature is decreased. In addition, as the temperature is increased, a shift of the Raman frequency, or change in linewidth can often be observed. The second two changes are of most interest to the experiments described here. Fig. 2 presents micro Raman spectra obtained from Si chips for different laser powers. The power was measured at the point where the laser light enters the microscope. The spectra show that at high powers, a second peak, in addition to the 520 Rcm^{-1} crystalline peak, at lower relative wavenumbers is present. When the power is decreased the second peak shifts toward the crystalline peak at 520 Rcm^{-1} . Due to the change in peak position and linewidth with incident power, it can be concluded that this peak is due to heated Si. The temperature of the chips can be deduced from the

Raman frequency and is given in Fig. 3 for the observed peak shifts and measured power into the microscope. A linear fit is made to the data points and can be extrapolated to the 520 Rcm^{-1} at 300 K.

2.4 Stress Measurement of Raman scattering modes

A frequency displacement of a peak in a Raman spectrum can often be directly related to the stress of the material. In general, a displacement of a crystalline peak to a lower relative wavenumber in the Stokes Raman spectrum indicates tension, and a displacement to a higher relative wavenumber indicates compression. If the stress is directional and the symmetry of the crystal is broken, the degeneracy of a degenerate vibration can be lifted.

The line shape and line width may convey information about the physical identity of the stresses. The theory of spectral line shape predicts that the line width is inversely proportional to the phonon lifetime and that the line shape can be described by a Lorentzian function:

$$I(\nu) = \frac{I_0}{1 + ((\nu_0 - \nu)/(.5\omega))^2} \quad (2.2)$$

Here I_0 is the maximum intensity, ν_0 is the central Raman frequency and ω is the line width. Homogeneous line broadening results from a reduction of phonon lifetime that can result from impurities and grain boundaries and results in an increase in linewidth.

Inhomogeneous line broadening is due to a distribution of the central Raman frequency within the collection volume of material. In this case, the peak can in theory be fitted as a distribution of Lorentzian peaks and the line then takes on a Gaussian shape:

$$I(\nu) = I_0 e^{(-1.6651(\nu_0 - \nu)/\omega)^2} \quad (2.3)$$

where I_0 is the maximum intensity, ν_0 is the central Raman frequency and ω is the line width.

In experimental analysis, for the highest accuracy, the Raman peaks are fitted to a Lorentzian function or a mix of Lorentzian and Gaussian functions to determine the center frequency and full width at half maximum. Stress measurement is usually deduced from the center position of the fitted Raman peak. However, a broadened peak could result from a distribution of stresses within the collection volume of material. In this case, the peak can in theory be fitted as a distribution of Lorentzian peaks enveloped within a Gaussian function. A broadened peak could also result from the lifting of the degeneracy in a mode (*i.e.* the splitting of a degenerate mode).

The stress required to initiate a structural transition is material dependent. High shear stresses can drive structural changes that will not occur through hydrostatic compression. Therefore, the nonhydrostatic component of the stress during machining and indentation could be significant to the observed changes. In our analysis we will pay some attention to stress that exhibits non-hydrostatic dependence.

2.5 Probing depth dependence on incident wavelength

The collection volume in the Raman scattering experiment is determined by the probing depth and the focusing resolution, which are dependent on the excitation wavelength.

The intensity of light decays in a material following the relationship:

$$I = I_0 e^{-\alpha z} \quad (2.4)$$

where I_0 is the incident intensity, α is the absorption constant, and z is the distance from the surface. Conventionally, the probing depth is defined at the point where $I = .37I_0$ and can therefore be calculated as $y = 1/2\alpha$, since the light travels both in and out of the material. The absorption coefficient, α , is dependent on the energy of the incident light and the imaginary component of the index of refraction of the material. In this simple analysis, it is assumed that α is the same for both the incident and Raman scattered light.

The intensity ratio versus probing depth for crystalline Si, 6H-SiC, and crystalline Si₃N₄ are provided in Fig. 5, and Table 3 for various incident wavelengths. UV light allows for surface sensitive probing of wide bandgap materials. For example, measurements of 6H-SiC can be obtained for absorption depths within 35 nm of the materials surface with UV light, and micro focusing optics allow for μm lateral resolution. 6H-SiC and $\beta\text{-Si}_3\text{N}_4$ are both transparent to visible light. The absorption constant will change for different domain sized crystal because the imaginary component of the index of refraction is changed. Therefore, these values will be modified. In addition, because of reflections at the interfaces, interface effects may modify the intensity decay.

2.6 References

1. R. Loudon, *Adv. Phys.* 13, 423 (1964).
2. J.E. Smith, Jr. M.H. Brodsky, B.L Crowder, and M.I. Nathan, *Phys. Rev. Lett.* 26, 642 (1971).
3. J.S. Lannin, L.J. Pilione, S.T. Kshirsagar, R. Messier, and R.C. Ross, *Phys. Rev. B* 26, 3506 (1982).
4. D.W. Feldman, J.H. Parker, Jr., W.J. Choyke, and L. Patrick, *Phys. Rev.* 170, 170 (1968).
5. D.W. Feldman, J.H. Parker, Jr., W.J. Choyke, and L. Patrick, *Phys. Rev.* 173, 787 (1968).
6. Priscilla J. Colwell and Miles V. Klein, *Phys. Rev. B* 6, 498 (1972).
7. A. Chehaidar, R. Carles, A. Zwick, C. Meunier, B. Cros, J. Durand, *Jour. Non-Crys. Sol.* 169, 37 (1994).
8. N. Wafa, S.A. Solin, J. Wong, and S. Prochazka, *J. Non-Crys. Solids* 43, 7 (1981).
9. R.J. Nemanich, S.A. Solin, R.M> Martin, *Phys. Rev. B* 23, 6348 (1981).
10. H. Richter, Z.P. Wang, L. Ley, *Solid State Commun.* 39, 625 (1981).
11. D.W. Feldman, J.H. Parker, Jr., W.J. Choyke, and L. Patrick, *Phys. Rev.* 170, 170 (1968).
12. K. Honda, S. Yokoyama, S. Tanaka, *J. Appl. Phys.* 85, 7380
13. "Handbook of optical constants", E.D. Palik, ed. (Academic, Orlando, Fla. 1985).

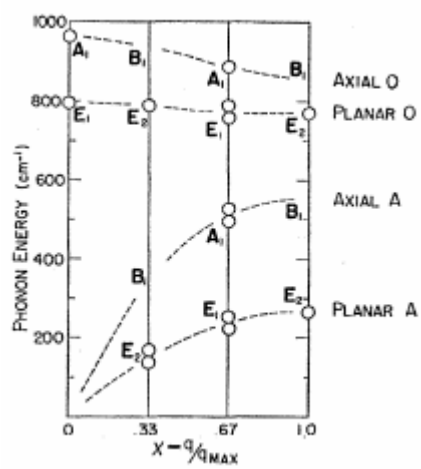


FIG. 1: The phonon dispersion curve for 6H-SiC in the large zone.¹¹

(a)			
	$\theta = 90^\circ$	$\theta = 45^\circ$	$\theta = 0^\circ$
L	E _{1l} 970	(A ₁ +E ₁) _t 967	A _{1t} (964)
T ₁	E _{1t} 797	E _{1t} 797	E _{1t} (797)
T ₂	A _{1t} 788	(A ₁ +E ₁) _t 792	E _{1t} (797)
(b)			
	$x = 0.33$	$x = 0.67$	$x = 1$
Axial optic	B ₁ , forbidden	A ₁ 967	B ₁ , forbidden
Planar optic	B ₁ , forbidden	A ₁ , not observed	
	E ₂ 788	E _{1t} 777	E ₂ 766
Axial acoustic	E ₂ , not observed	E _{1t} 769	
	B ₁ , forbidden	A ₁ 508	B ₁ , forbidden
Planar acoustic	B ₁ , forbidden	A ₁ 504	
	E ₂ 149	E _{1t} 241	E ₂ 262
	E ₂ 145	E _{1t} 236	

TABLE 1: The vibrational frequencies are given for (a) propagation angles relative to the c -axis and (b) the weaker modes are valid for any propagation direction and are assigned to values of $x = q / q_{\max}$ in the large zone. All values are experimental except the figures in parenthesis, which are calculated.¹¹

A_g	E_{2g}	A_g	E_{1g}	E_{2g}	E_{2g}	A_g	E_{1g}	E_{2g}	A_g	E_{2g}
145	185	208	230	452	620	733	866	930	940	1048

TABLE 2: Backscattering first-order Raman scattering active modes of β - Si_3N_4 in Rcm^{-1} .¹²

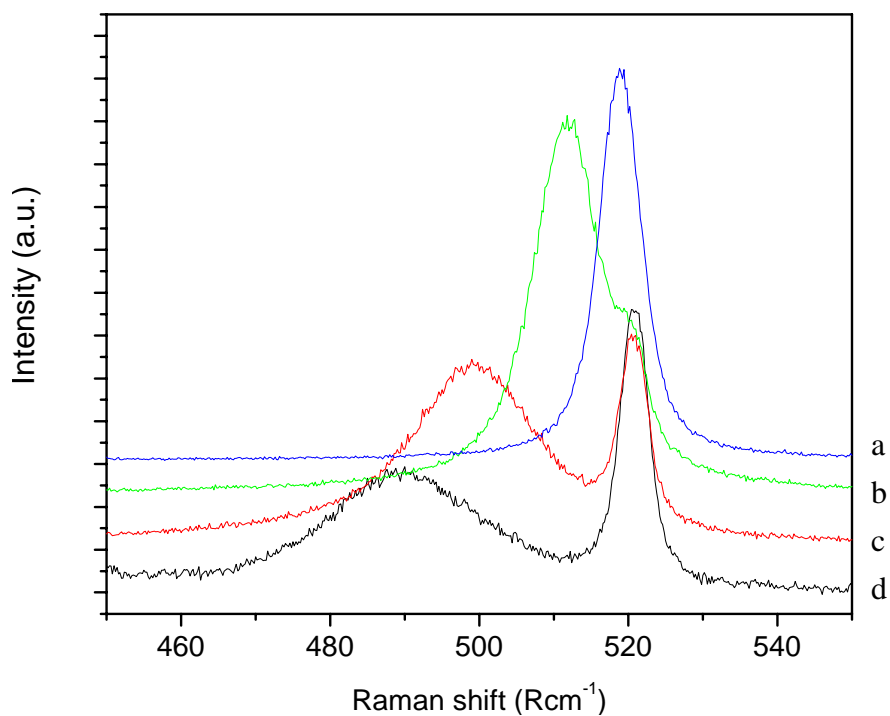


FIG. 2: Micro Raman scattering of Si chips showing the crystalline Si peak at 520 Rcm^{-1} and a heated peak at lower relative wavenumbers. The spectra (a) to (d) are from lower to higher power, respectively.

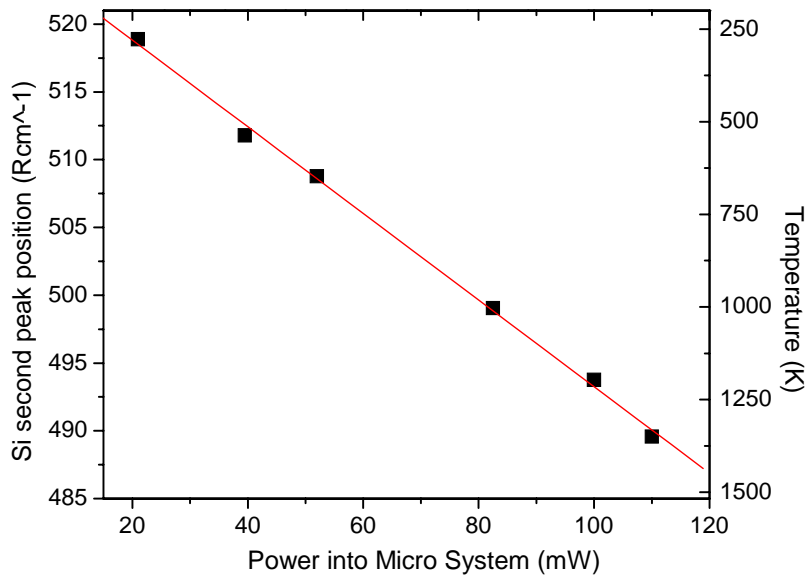


FIG. 3: The peak position of the Raman scattering spectra from Si chips versus laser power. The vertical scale on the right represents the temperature that would correspond to the observed Raman scattering peak shift.

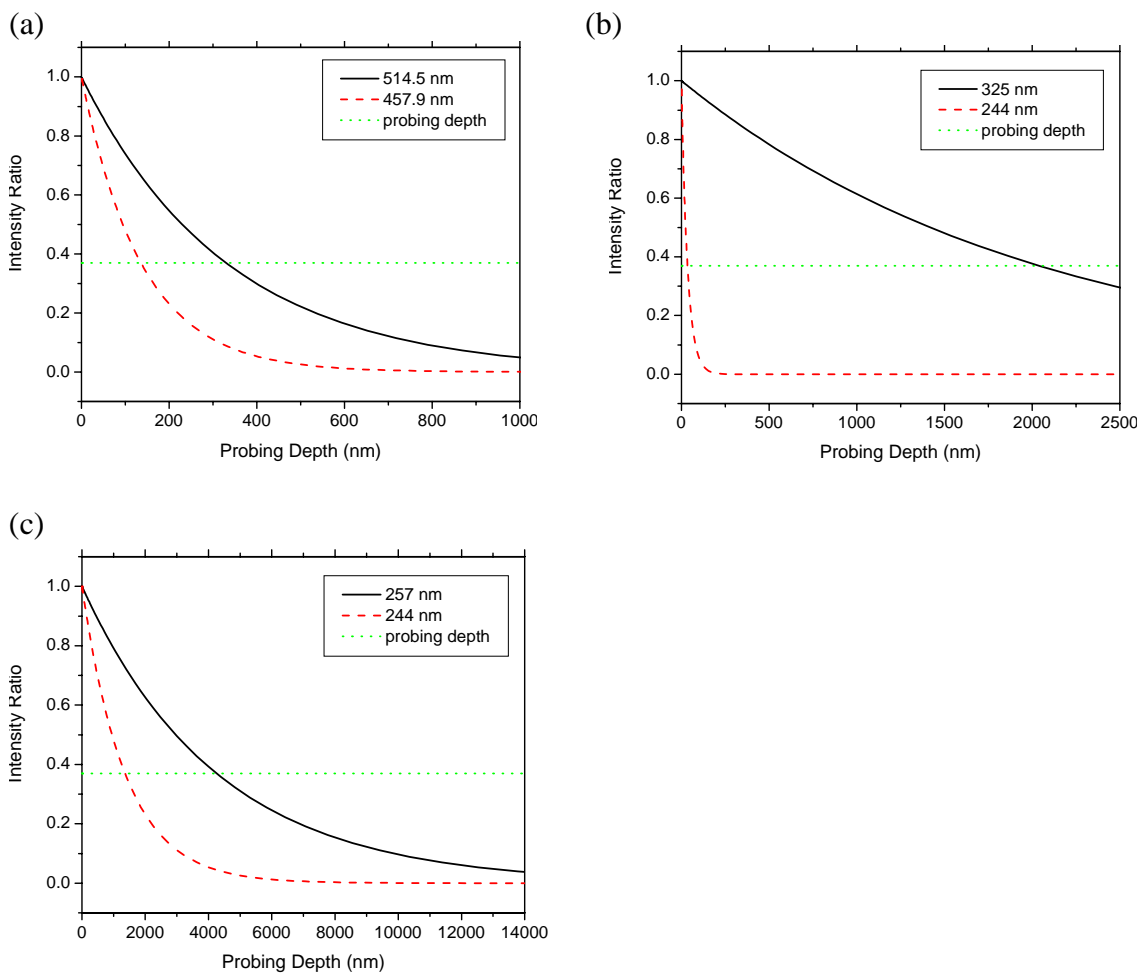


FIG. 4: Decay of the Raman scattering signal with depth in the sample for (a) single crystal Si (b) single crystal 6H-SiC and (c) β -Si₃N₄.¹³ The probing depth is defined as the depth where the intensity is 37% of the incident intensity.

Probing Wavelength (nm)	Probing depth Si (nm)	Probing depth 6H- SiC (nm)	Probing depth β - Si ₃ N ₄ (nm)
244	--	34.72	1366
257	--	80.39	4273
325	--	2050	--
488	247.2	transparent	transparent
514.5	331.6	transparent	transparent

TABLE 3: Calculated probing depths for single crystal Si, single crystal 6H-SiC, and β -Si₃N₄.¹³ The probing depth is defined as the depth where the intensity is 37% of the incident intensity.

3. Transformations in Si, SiC and Si₃N₄

3.1 Transformation Process

Under high pressures, a crystal may experience a structural transformation where there is a sudden change in the arrangement of the atoms. If the displacement of the lattice is discontinuous, or continuous with a change in symmetry, then the transition is said to be a phase transformation. Since the Gibbs free energies of the different possible arrangements of atoms vary under compression, a phase transformation will occur at a point where it becomes favorable for the material to change the type of atomic arrangement. Phase transitions can be classified as reconstructive transitions, which include breaking and forming of bonds, or as displacive transitions in which the positions of the atoms are changed by small amounts. There are a multitude of identified phases of Si, Si₃N₄ and SiC, and many of their crystallographic transformations have been investigated. Within each crystallographic structure, the number of atoms per unit cell can vary resulting in different polytype. For example, there are more than 200 identified different stacking sequences or polytypes in SiC. Applied pressures can cause transformation between the phases and upon releasing the pressure, the material can relax to a different phase or even a metastable state. Since the free energies are often very close to each other at a given temperature, it is possible for relaxation to several different structures. In addition, the lifetime of the metastable phases can be material dependent. Because of the rapid change in pressure, it is common for transformation back from the high-pressure metallic phase to result in one of the higher energy or metastable phases. Therefore, measurement of higher energy residual states on precision engineered and

machined surfaces provides evidence that the material may have relaxed from a metallic or another denser phase.

Extensive investigations of Si have indicated transformations to different residual phases for diamond anvil cell pressures and point pressures where the residual metastable phases are dependent on the rate of decompression.¹ Conversely, investigation of the high-pressure phases and phase transformations of SiC and Si₃N₄ have been limited.

3.2 Transformations in Si

Wide ranges of study from experiments and calculation have determined the structures of Si under high pressures. Under nearly hydrostatic conditions, Si-I transforms to Si-II (β -tin) in the pressure range of 9 to 16 GPa.^{2, 3, 4, 5} The metallic β -Sn phase transforms to a phase with Imma symmetry at ~13.2 GPa, and the Imma phase transforms to a simple hexagonal (sh) phase at ~15.4 GPa.⁶ At ~38 GPa the sh phase transforms to a base-centered orthorhombic structure with Cmca symmetry, and at ~42 GPa the Cmca phase transforms to a hexagonal closed packed (hcp) structure.⁷ At about ~80 GPa the hcp transforms to a face centered cubic (fcc) phase.⁸

At room temperature the transition to the high temperature phase and the transitions after pressure release are typically different. The high-pressure phase found to decompress to the metallic β -Sn phase during relaxation.⁹ Upon further relaxation, the Si-II metallic phase transforms to different metastable phases, which are dependent on pressure release conditions. For slow decompression at 10-12 GPa Si-XII (*r8* rhombohedral)^{10, 11} is

formed, and on further pressure release, the degree of rhombohedral distortion diminishes gradually, producing a mixture of Si-XII and Si-III (*bc8* body-centered cubic).^{12, 13} The Si-XII is found to persist to ambient pressure. For fast decompression, an amorphous Si phase can result.^{14, 15} Annealing will result in the transformation back to the Si-I parent phase.

3.3 Transformations in SiC

The lattice planes of SiC are composed of Si-C double layers that are parallel to the (0001) plane, and the packing axis is along the [0001] face. SiC is predicted to compress to a metallic^{16, 17, 18} or rocksalt^{19, 20, 21, 22} phase, but the mechanism of transformation is not well understood. Experiments have indicated a phase transition in 3C-SiC (zb structure) to a rocksalt (NaCl) phase at ~100 GPa.²³ Theoretical first principle LDA calculations indicate that the NaCl form becomes favorable at pressures of ~66 GPa.²⁴ In addition, a phase transition of 6H-SiC to an undetermined phase has been reported subject for shock compression.²⁵ Analyses of the specific phases that result from pressure release are limited for this material.

Polytypism originates from differences in the stacking sequences of the silicon-carbon pair hexagonal layers and may be arrayed in the cubic, hexagonal, or rhombohedral crystal structures. Numerous studies have been reported on transformations between polytypes as a function of temperature and/or pressure by both solid-state mechanisms and diffusion processes.^{26, 27} For example, a TEM study of indentations performed at 1170°C on 6H-SiC ($\bar{1}100$) reported strong deformation and kinking, which produced

polycrystalline material, and it was observed that some of the grains undergo transformation from the 6H-SiC structure to the 3C-SiC structure through the formation of Shockley partial dislocations lying on the cross-slip plane.²⁸ In a six-layer period of the 6H-polytype, which consists of two three layered microtwins, one of the microtwins can be untwinned by the passage of three partial dislocations with the same $\frac{1}{2} \langle 1010 \rangle$ Burgers vector, thus converting the 6H period into two identical 3C periods. The dislocation model for the transformation requires a pinned segment of a screw dislocation that dissociates into two 30 degree partials on the basal plane, a temperature range where there is a large difference in the mobility of the two 30 degree partial dislocations, a sufficiently high resolved shear stress on the primary glide plane to form a faulted loop from the highly mobile leading partial, and a sufficiently large resolved shear stress on the cross-slip plane to make the screw dislocation cross-slip after it has been formed.

To demonstrate the differences in Raman spectra for the various polytypes, Fig. 1 shows the Raman spectra of 4H-SiC, 6H-SiC, and a sample that contained a mixture of 4H-SiC and an unknown polytype.

3.4 Transformations in β -Si₃N₄

Transformation of Si₃N₄ is similar to that of SiC in the sense that the stacking sequence can be used to describe the differences between their crystal structures. The crystal structure of β -Si₃N₄ consists of two layers of silicon and nitrogen atoms stacked along the [0001] direction. Each silicon atom is positioned at the center of a distorted tetrahedron, and nitrogen atoms are placed in the corners with stacking sequence ABAB.

Investigations of the high-pressure phases of β - Si_3N_4 are very limited. However, preliminary diamond anvil cell experiments conducted by a member of our group (Patten) has revealed low energy x-ray diffraction peaks at pressures between 20 GPa and 35 GPa, which are a signature of the high pressure phase of silicon nitride.²⁹ The diffraction peaks were shifted to smaller angles indicating that the transformed material was denser than the starting phase.

The crystal structure of β - Si_3N_4 consists of four layers with stacking sequence ABCDABCD. To form the α to β transition in Si_3N_4 , layer C must be changed to layer A and layer D must be changed to layer B, which would require a rotation of 60° of the silicon-centered tetrahedral. Therefore, a direct transformation and reconstruction of the crystal from the α to the β phase is usually associated with short-range diffusion rather than the translation, which would require nonuniform displacement vectors.³⁰

References

1. V. Domnich, Y. Gogotsi, *Experimental Methods in the Physical Sciences* 38, 355 (2001).
2. H. Olijnyk, S.K. Sikka, and W.B. Holzapfel, *Phys. Lett. A* 103, 137 (1984).
3. S. Minomura and H.G. Drickamer, *J. Phys. Chem. Solids* 23, 451 (1962).
4. J.C. Jamieson, *Science* 139, 762 (1963).
5. J.Z. Hu, L.D. Merkle, C.S. Menoni, I.L. Spain, *Phys. Rev. B* 34, 4679 (1986).
6. S.P. Lewis, M. L. Cohen, *Phys. Rev. B* 48, 16144 (1993).
7. N. E. Christensen, D.L. Novikov, M. Methfessel, *Solid State Commun* 110, 615 (1999).
8. R. J. Needs, A. Mujica, *Phys. Rev. B* 51, 9652 (1995).
9. B. G. Pfrommer, M. Côté', S.G. Louie, M.L. Cohen, *Phys. Rev. B* 56, 6662 (1997a).
10. J. Crain, G.J. Ackland, J.R. Maclean, R.O. Piltz, P.D. Hatton, and J. Crain, *Phys. Rev. B* 50, 13043 (1994).
11. R.O. Piltz, J.R. Maclean, S.J. Clark, G.J. Ackland, P.D. Hatton, and J. Crain, *Phys. Rev. B* 52, 4072 (1995).
12. R.H. Wentorf and J.S. Kasper, *Science* 139, 338 (1963).
13. J. S. Kasper and S.H. Richards, *Acta Crystall.* 17, 752 (1964).
14. D.R. Clarke, M.C. Kroll, P.D. Kirchner, R.F. Cook, B.J. Hockey, *Phys. Rev. Lett.* 60, 2156 (1988).
15. D.L. Callahan and J.C. Morris, *J. Mater. Res.* 7, 2907 (1992).
16. J. A. Van Vechten, *Phys. Rev. B* 7, 1479 (1973).
17. J. R. Cheilowsky and J. K. Burdett, *Phys. Rev. Lett.* 56, 961 (1986).
18. J. R. Chelikowsky, *Phys. Rev. B* 35, 1174 (1987).

19. N.E. Christensen, S. Satopathy, and Z. Pawlowska, *Phys. Rev. B* 35, 1032 (1987).
20. K. J. Chang and M. L. Cohen, *Phys. Rev. B* 35, 8196 (1987).
21. B.H. Cheong, K.J. Chang, and M.L. Cohen, *Phys. Rev. B* 44, 1053 (1991).
22. A. Garcia and M. L. Cohen, *Phys. Rev. B* 47, 4215 (1993).
23. M.A. Yoshida, M. Onodera, M. Ueno, K. Takemura, and O. Shimomura, *Phys. Rev. B* 48, 10587 (1993).
24. K. J. Chang and M.L. Cohen, *Phys. Rev. B* 35, 8196 (1987).
25. T. Sekine, T. Kobayashi, *Phys. Rev. B* 55, 8034 (1997).
26. P. Krishna, R.C. Marchall, and C.E. Ryan, *J. Crystal Growth* 8, 129 (1971).
27. G.A. Bootsma, W.F. Knippenberg, and G. Verspui, *J. Crystal Growth* 8, 341 (1971).
28. J. W. Yang and P. Pirouz, *J. Mater. Res.* 8, 2902 (1993).
29. C. Ullner, J. Beckmann, and R. Morrel, *J. Eur. Ceram. Soc.* 22, 1183 (2003).
30. Hisayuki Suematsu, Mamoru Mitomo, Terence E. Mitchell, John J. Petrovic, Osamu Fukunaga, Naoki Ohashi, *J. Am. Ceram. Soc.* 80, 3 615 (1997).

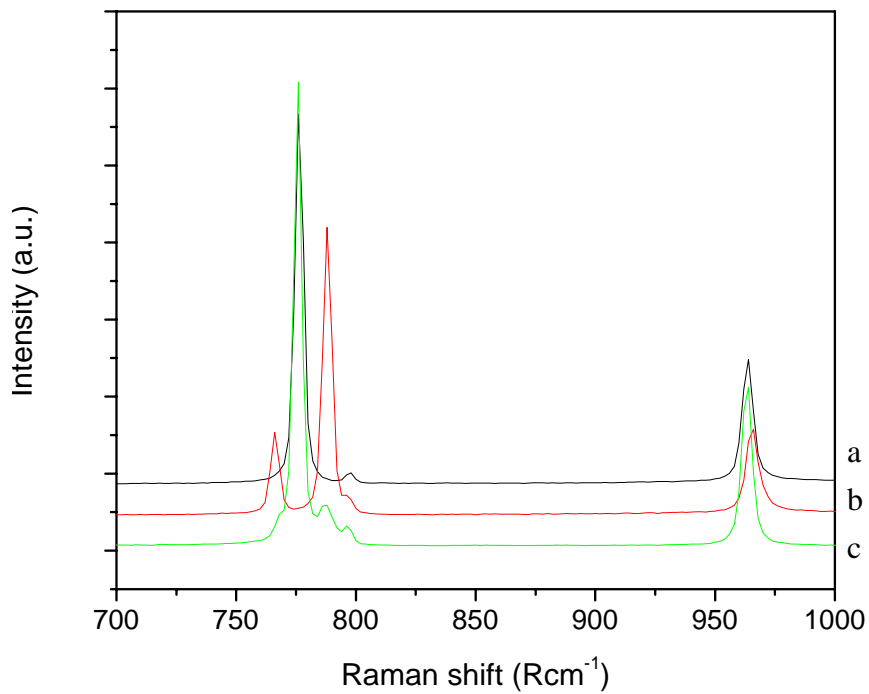


FIG 1: Micro Raman scattering spectra of three SiC wafers which show the dominant TO modes at $\sim 760\text{Rcm}^{-1}$ and the LO modes at $\sim 970\text{Rcm}^{-1}$ for (a) 4H-SiC, (b) 6H-SiC, and (c) a mixture of 4H and 6H SiC.

4. Raman Scattering Analysis of Indented and Machined Si

Jennifer J.H. Walter,¹ Travis Randall,¹ Jae-il Jang,^{2,3} George M. Pharr,^{2, 3} Ronald O. Scattergood,¹ Robert J. Nemanich¹

¹*North Carolina State University, Raleigh, NC 27695*

²*University of Tennessee, Knoxville, TN 37996*

³*Oak Ridge National Laboratory, Oak Ridge, TN 37830*

4.1. Experiment Summary

It has been well documented that Si will plastically deform without fracture from the highly localized pressures during μm and nm indentation and machining. A phase transformation during machining to a high-pressure metallic $\beta\text{-Sn}$ phase is thought to be responsible for the anomalous plastic flow. In comparison to the directional, covalent bonding of Si, which gives this material its brittle properties, the non-directional bonding of the metallic phase may prevent brittle fracture. A high-pressure metallic phase obtained from point pressures in Si has been indicated with increases in conductivity during microhardness tests.¹ However, due to the complexity of deformation from localized pressures, the mechanisms of pressure induced plastic flow are not well understood. The response of the material can be influenced by a combination of microcracking, dislocation motion, and phase changes to harder phases, in addition to a phase change to a metallic phase. This study employs macro and micro Raman spectroscopy to explore the residual phases that result from indented Si (001), and machined Si (001) and Si (111) surfaces. The residual phases provide evidence of a high-pressure metallic phase transformation. The indented surfaces provide a controlled method to study plastic flow from point pressure, thus gaining insight into the mechanisms of ductile machining.

4.2 Experiment Details

The indentation experiments were performed on a single crystal Si (001) wafer. The machining experiments were performed on single crystal Si (111) and Si (001) wafers.

The indentations were made using a Nanoindenter-XP (MTS, Oak Ridge, TN). A Berkovich diamond indenter tip shaped as a three-sided pyramid with a centerline-to-face angle, Ψ , of 65° was used to create triangular shaped indentations. The tip was brought into contact with the material with loads of 100, 200, and 700 mN, and at a constant loading rate 5 mN/sec.

A Rank Pneumo ASG 2500 Diamond Turning Machine was used to turn various orientations of the silicon wafers at room temperature as a function of feed rate from 1 to 15 $\mu\text{m}/\text{rev}$. The rate is defined as the distance traveled inward or outward across the wafer surface per revolution. Tool rake angles of -30° and -45° were employed with a 3mm radius rounded tool. Machining runs on Si were subject to tip wear and damage considerations as evidenced by the repeated patterns of tip damage features displayed into the machined part surface. However, tool wear was not considered to be an issue since surfaces turned within the ductile regime had RMS values in the range of 1 to 10 nm. The lower RMS roughness values corresponded to the low feed rates, and the higher RMS roughness values corresponded to high feed rates.

The Raman scattering experiments were performed with both macro and micro focusing capabilities. In the macro system, a $\sim 45^\circ$ backscattering geometry was employed and a

spot size of $\sim 100 \mu\text{m} \times \sim 2 \text{mm}$ was focused on the sample. In the micro system, a 180° backscattering geometry was employed and a spot size of $\sim 2 \mu\text{m}$ was incident on the sample. The Raman experiments were performed with the 514.5 nm line of an argon ion laser (Coherent Inc.), and the scattered light was focused onto the entrance slit of a double grating scanning monochromator (ISA U-1000). For measurements on the Si (001) surfaces, careful attention was given to keeping the crystal orientation relative to the polarization of the incident laser light consistent, which will allow comparison of amorphous and crystalline peaks.

4.3 Results

A. Indents

Indentation experiments were performed on a Si (001) surface to investigate local bonding arrangements from controlled point pressure conditions. The load displacement curves for maximum indentation loads of 100 and 200 mN, and an indentation rate of 5 mN/s are provided in Fig. 1. A pop-out feature in the unloading portion of the curve is detected for the 100 mN load. A smaller pop-out feature is also observed for the 200 mN in the load displacement curve. These features have previously been explained by a phase transition accompanied by a volume change in the Si structure.³

SEM images of the Si indentations for maximum indentation loads of 100, 200, and 700 mN are shown in Fig. 2. The figures illustrate the impressions left on the surface and the debris surrounding the deformed region. The region of the 700 mN indentation appears

highly cracked while the indented region of the 200 mN load indicate limited cracking. The indented regions of the 100 mN indent indicates no evident macro cracking.

The Raman scattering spectra of the 200 and 700 mN indentations are provided in Fig. 3. The 200 mN indent indicate additional peaks with the center positions located at 352, 375.5, 384, and 434 Rcm^{-1} . The Raman peaks positions have been previously assigned to Si III and Si VII.⁴ There is also a small, broadened peak indicated at 480 Rcm^{-1} . This peak is commonly assigned to amorphous Si. The 520 Rcm^{-1} crystalline peak is displaced to higher relative wavenumbers to a center frequency of 522 Rcm^{-1} . This peak displacement indicates residual compressive stress in the indent. The 700 mN load indent indicates a crystalline peak with center frequency at 520 Rcm^{-1} and a second peak shifted to lower relative wavenumbers at 513 Rcm^{-1} . At lower powers it is shifted toward the crystalline Si peak at 520 Rcm^{-1} . Thus indicating that this second peak at lower wavenumbers is due to laser heating of the cracked regions and the chips surrounding the indent.

B. Machined Surfaces

The machined Si (111) surface indicated a ductile to brittle transition that is dependent on the crystallographic direction of the wafer face. After machining, symmetric damage patterns were created on the surface. An orientation stress model has been proposed to qualitatively explain the damage patterns.⁵ Fig. 4 presents the schematic of the damage patterns, which is generalized for (001) and (111) surfaces of diamond cubic structures. Here, the close-hatched regions represent severe damage, the hatched regions represent

mild damage, and the white areas represent ductile regions. The damage patterns observed on the Si machined surfaces are in agreement with the predicted fracture pattern with this model. On our machined surfaces, the surface areas of the ductile regions were found to increase with slower feed rates and for larger negative rake angles.

Fig. 5 presents macro Raman scattering spectra obtained from a machined Si (111) wafer for feed rates of 5 and 1 $\mu\text{m}/\text{rev}$. A rake angle of -45° was employed, and the spectra were obtained from the $[\bar{1}\bar{1}0]$ wafer direction. This direction corresponds to a ductile region of the wafer. A significant decrease in the crystalline Si peak, and an increase in the amorphous peak are observed.

Fig. 6 presents the Raman scattering spectra of a machined Si (001) surface for feed rates ranging from 15 to 1 $\mu\text{m}/\text{rev}$. The intensity of the crystalline Si (001) peak at 520 Rcm^{-1} is dependent on the polarization of the incident light relative to the orientation of the materials surface. In this experiment, the sample was oriented to minimize the intensity of the crystalline Si peak, thus allowing for comparison of the peaks. In comparison to the machined Si (111) surface, a consistent decrease in the Si crystalline peak and correspondingly relative increase in the amorphous component is also indicated from the machined Si (001) Raman scattering spectra. The spectra indicate that within this range of results, a lower cutting rate produces a larger amorphous extent than the higher cutting rate.

Macro Raman scattering measurements of a machined Si (111) surface for rake angles of -45° and -25° are provided in Fig. 7. The machining rate was $1 \mu\text{m}/\text{rev.}$, and for the $[\bar{1}\bar{1}0]$ wafer direction. This direction corresponds to a ductile region of the wafer. Both rake angles show the presence of a 480 Rcm^{-1} feature indicating an amorphous layer and the 520 Rcm^{-1} crystalline Si peak, however, the peak intensity ratios of amorphous to crystalline Si is found to be greater for the larger negative rake angle. This indicates that the amorphous surface layer is greater for a larger negative rake angle.

Fig. 8 shows macro Raman scattering spectra of machined Si (111) surfaces obtained with a rake angle of -45° and a feed rate of $1 \mu\text{m}/\text{rev.}$ The spectra were obtained along the $[\bar{1}\bar{1}0]$, $[\bar{1}\bar{1}\bar{2}]$, and $[11\bar{2}]$ wafer directions. The wafer directions correspond to ductile regions of the wafer. The Raman scattering spectra indicate no significant difference in the extent of the amorphous layer for these difference directions.

4.4 Discussion

SEM images of the Si indented surfaces for the 100 mN and the 200 mN maximum loads indicate limiting cracking. The Raman scattering measurements indicate Si III and Si VII metastable phases for the 100 and 200 mN load indents. A peak shift to higher relative wavenumbers indicates compression in the surrounding Si lattice. SEM images of the 700 mN high load indent indicate that the surface is highly cracked. The Raman scattering measurements indicate no evidence of other phases, and there was no observed stress. It has been proposed that at larger loads the volume of displaced material is larger, and dislocation slip around the compacted volume may become necessary to

accommodate the necessary displacements.⁶ Therefore, a maximum load threshold exists where fracture and cracking become dominant over a phase transition.

On the machined Si surfaces, a ductile and brittle response is found to have orientation dependence on the wafer surface relative to the machining tool. Machining with lower machining rates increased the surface areas of ductile material. Raman scattering of the ductile-machined surfaces does not indicate significant differences in the amorphous layer thickness for the ductile-machined crystal orientations. However, the Raman scattering measurements of the ductile turned surfaces indicated an amorphous layer that was thinner for higher feed rates, and also for smaller negative rake angles. The extent of the amorphous layer is greater when machining at a lower rate. A plausible explanation for a thinning layer with increased feed rate is that more material is machined away as debris. The extent of the amorphous layer is found to be greater for larger negative rake angles. This could be due to higher pressures generated at the contact interface between the machining tool and the material for larger negative rake angles. In addition, with increased feed rates and smaller negative rake angles, it was found that the fractured surface regions increase, while the surface area of ductile response decreases. This effect can be explained with the stress orientation model for diamond cubic surfaces.⁷

These residual phases measured on the ductile surfaces are evidence of a high-pressure phase transformation to a metallic phase. Prior hydrostatic pressure studies of Si in diamond anvil cells indicate that the high-pressure metallic phase will decompress to different metastable, or amorphous phases, upon pressure release.² The high-pressure

metallic phase could explain the ductile response observed from point pressure on this brittle material.

4.5. Conclusions

The studies indicate that point pressures on Si surfaces can produce a ductile response. Residual metastable and amorphous phases and stresses are measured on the indented and machined ductile surfaces. There is no evidence of residual phases on the cracked, brittle surfaces. On machined surfaces, damage patterns can be predicted with a stress model that is based on fracture of the crystal planes. The ductile surfaces indicate a residual amorphous surface layer and the brittle surfaces indicate a crystalline structure. The machining wafer directions that indicate a ductile response do not show a significant dependence on extent of the amorphous layer for the different crystal orientations. However, the extent of the amorphous layer is found to change as a function of material removal rate and tool rake angle. For increased material removal rates, the amorphous layer was thinner. This could be due to the ductile material on the surface machined away as debris. For larger negative rake angles the amorphous layer was also found to be thinner. This could be due to a higher generation of the metallic phase created at the contact interface during machining due to the higher pressures. The metastable and amorphous phases of the ductile machined indentations and machined surfaces are evidence relaxation of a high-pressure metallic phase, which could explain the origin of the ductile response of Si subjected to point pressures.

4.6 References

1. D. R. Clarke, M.C. Kroll, P.D. Kirchner, R.F. Cook, *Phys. Rev Lett.* 60, 2156 (1998).
2. H. Olijnyk, S.K. Sikka, and W.B. Holzapfel, *Phys. Lett. A* 103, 137 (1984).
3. V. Domnich, Y. Gogotsi, S. Dub, *Appl. Phys. Lett.* 76, 16 2214 (2000).
4. V. Domnich, Y. Gogotsi, *Experimental Methods in the Physical Sciences* 38, 355 (2001).
5. W.S. Blackley and R.O. Scattergood, *J. Am. Ceram. Soc.* 73, 10 3113 (1990).
6. S.V. Hainsworth, A.J. Whitehead, and T. F. Page, in “Plastic Deformation of Ceramic” (R.C. Bradt, C.A. Brooks, and J.L. Routburt, Eds.) 173, Plenum Press, NY (1995).
7. W.S. Blackley, R. O. Scattergood, *J. Am. Ceram. Soc.* 73, 3113 (1990).

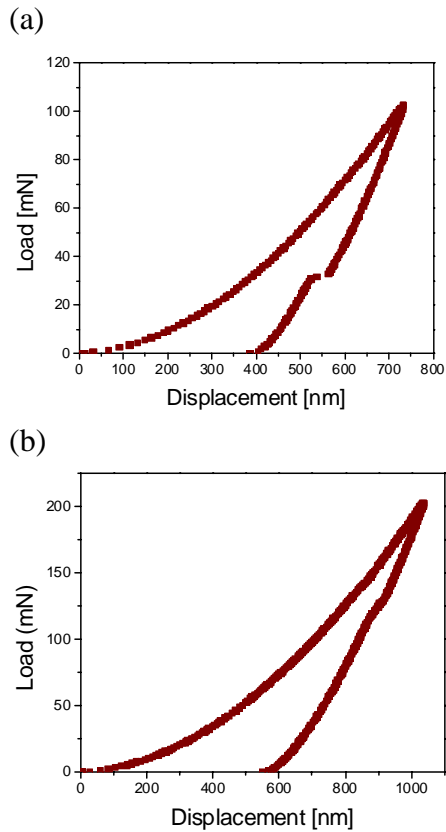


FIG 1: One step load displacement curves for (a) 100 and (b) 200 mN maximum load indents. An indentation rate of 5 mN/s was employed.

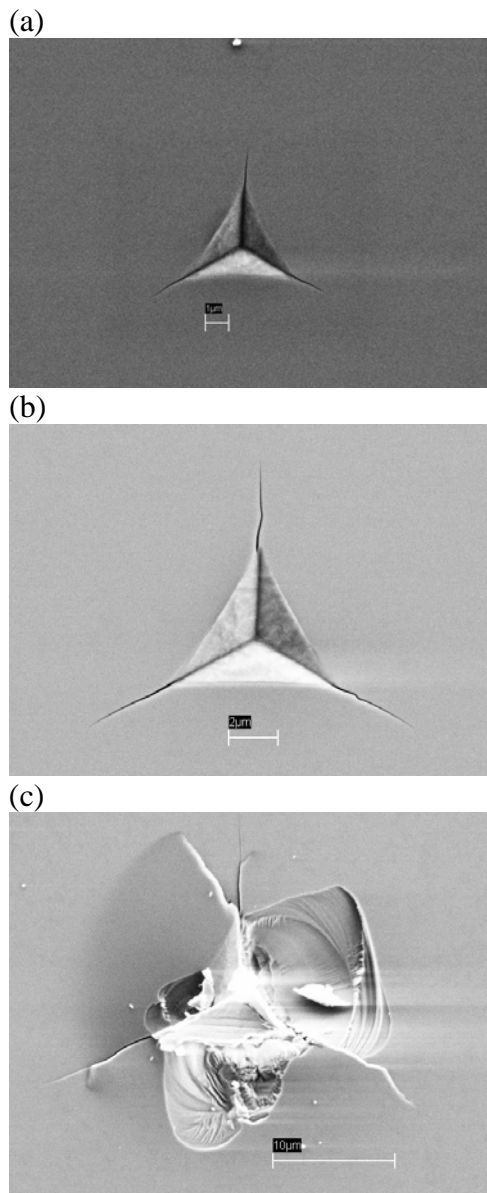


FIG 2: SEM images of Si indentations for maximum loads of (a) 100, (b) 200, and (c) 700 mN. An indentation rate of 5 mN/s was employed.

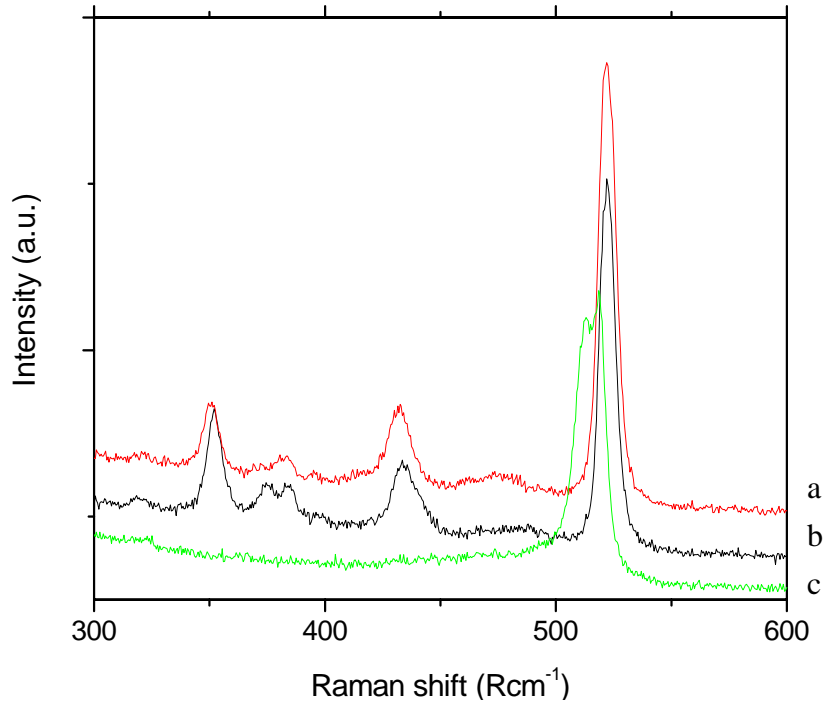


FIG 3: Micro Raman scattering spectra taken from the center of a Si indentation obtained with a maximum load (a) 100, (b) 200, and (c) 700 mN.

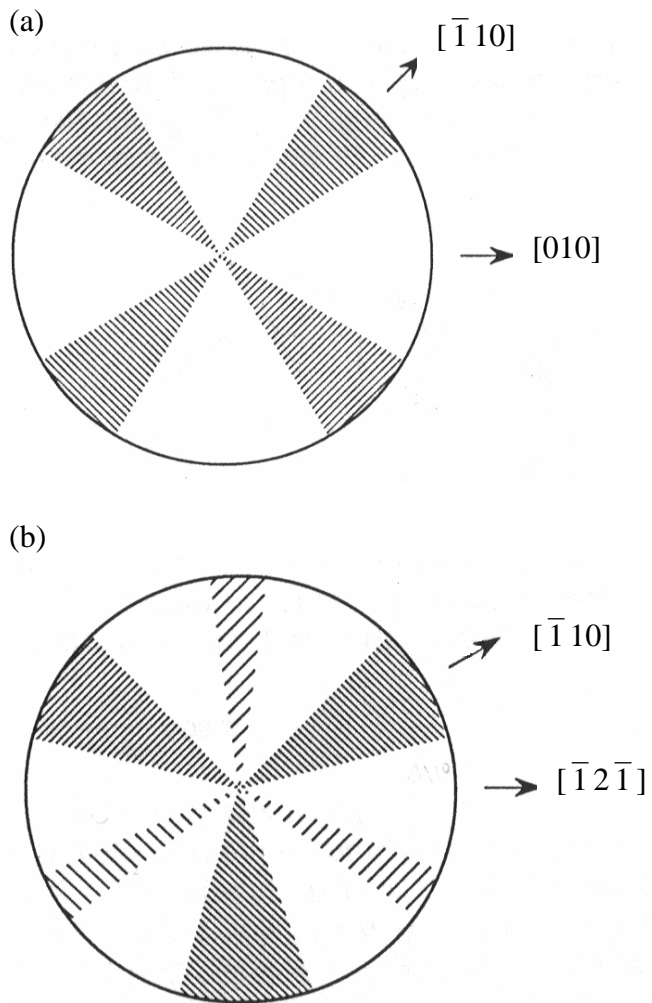


FIG 4: Schematic of the typical damage pattern observed from machined (001) and (111) surfaces of a diamond cubic lattice.⁷

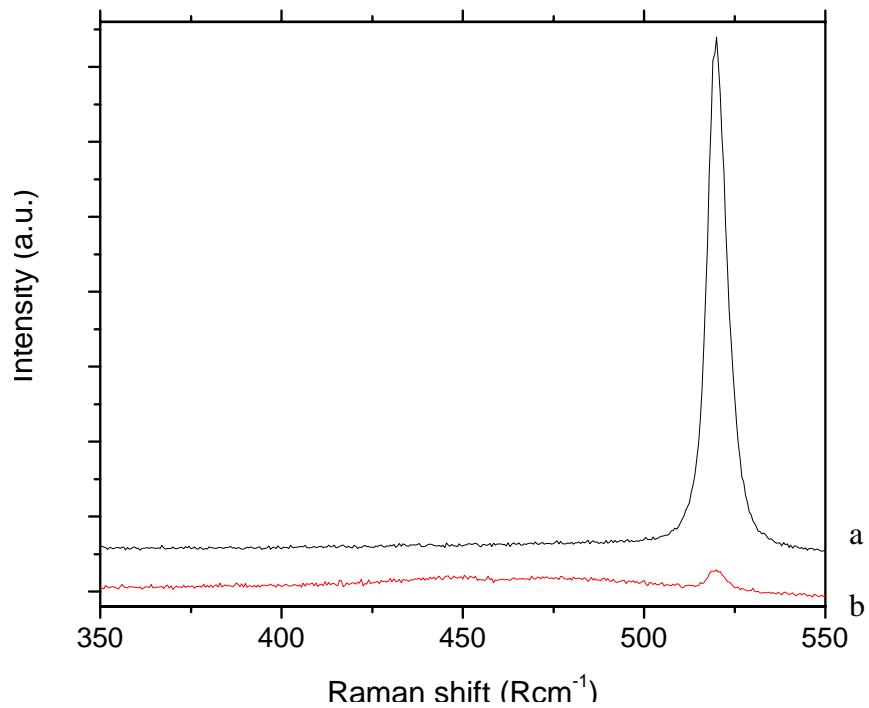


FIG 5: Macro Raman scattering spectra of machined Si (111) wafer machined in the $[1\bar{1}0]$ direction with a rake angle of -45° and with a feed rate of (a) 5 and (b) 1 $\mu\text{m}/\text{rev}$.

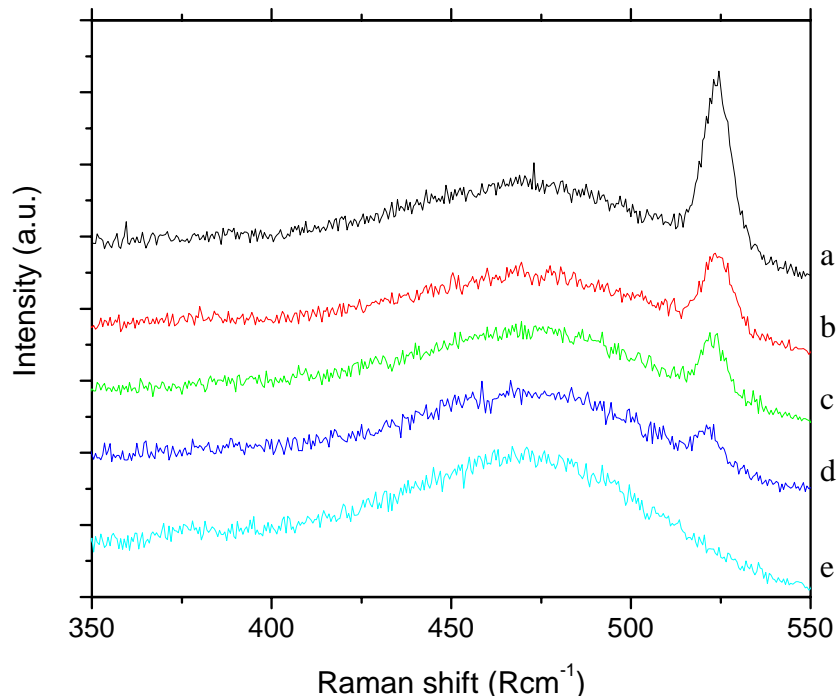


FIG 6: Macro Raman scattering spectra of machined Si (001) surfaces for rates varying from (a) 15 (b) 7 (c) 3 (d) 2 to (e) 1 $\mu\text{m}/\text{rev}$. The surfaces were machined in the [010] direction.

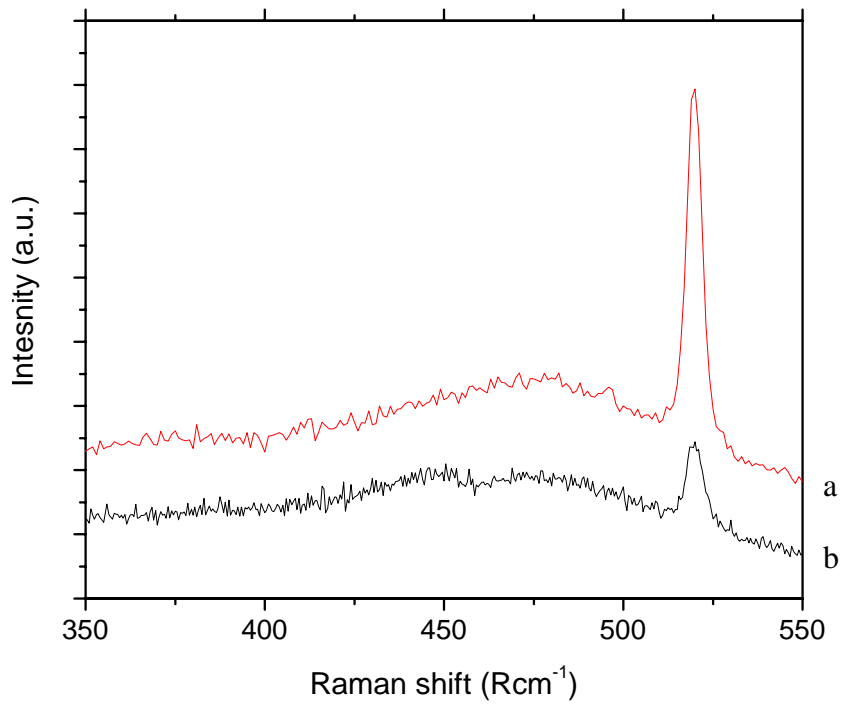


FIG 7: Macro Raman scattering spectra of machined Si (111) surfaces with a rake angle of (a) -25° and (b) -45° . The machining rate was $1 \mu\text{m}/\text{rev.}$, and the direction of cut was along [110].

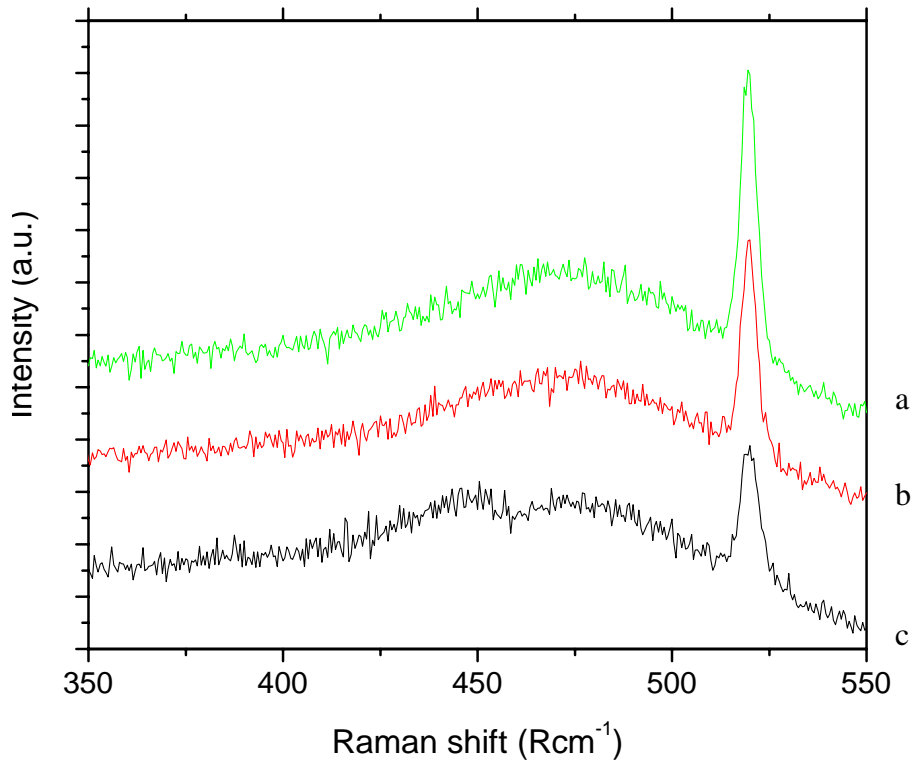


FIG 8: Macro Raman scattering spectra of a machined Si (111) wafer with a rake angle of -45° and feed rate $1 \mu\text{m}/\text{rev}$. for ductile machining wafer directions of (a) $[1\bar{1}0]$, (b) $[\bar{1}\bar{1}2]$, and (c) $[11\bar{2}]$.

5. UV Raman Scattering Analysis of Indented and Machined 6H-SiC

Jennifer J.H. Walter,¹ Jae-il Jang,^{2,3} George M. Pharr,^{2,3} Xiang-Bai Chen,⁴ Leah Bergman,⁴ John A. Patten,⁵ Robert J. Nemanich¹

¹*North Carolina State University, Raleigh, NC 27695*

²*University of Tennessee, Knoxville, TN 37996*

³*Oak Ridge National Laboratory, Oak Ridge, TN 37830*

⁴*University of Idaho, Moscow, ID 83843*

⁵*University of Western Michigan, Kalamazoo, MI 49008-5314*

5.1. Experimental summary

The local bonding structures of indented 6H-SiC (0001), and precision-machined single crystal 6H-SiC (0001) circular wafer edges are analyzed with UV Raman spectroscopy. The measurements were obtained with the 244 nm excitation resulting in absorption depths of 35 nm. Moreover, focusing optics allow for μm lateral resolution. To explore the residual structural changes of 6H-SiC ductile surfaces, controlled studies have been conducted on indentations made on a 6H-SiC (0001) surface. The indented surfaces indicate limited macro cracking. Raman scattering measurements indicate that the plastically deformed indented regions are highly stressed. Furthermore, studies of machined 6H-SiC (0001) wafer edges indicate ductile, and brittle regions, which are dependent upon the 6-fold symmetry of the wafer edges. Raman scattering measurements of the ductile regions indicate a polycrystalline surface layer. The polycrystalline structure may be the relaxed structure of the high-pressure metallic phase, thus explaining the origin of the ductile response observed from this material.

5.2 Experimental details

The 6H-SiC samples used for indentation were supplied by Cree Inc., and the wafers used

for machining were purchased from SiCrystal AG. The wafers are circular with a 50 mm diameter, and 250 μm thickness. Both the indented, and machined SiC wafers were transparent to visible light, and had a light green color.

The indentation experiments were performed on a polished (0001) 6H-SiC surface using a Nanoindenter – XP (MTS, Oak Ridge, TN). This surface corresponds to the Si-face of an ideally terminated structure. A Berkovich diamond indenter tip shaped as a three-sided pyramid with a centerline-to-face angle, Ψ , of 65° was used to create triangular shaped indentations. The tip was brought into contact with the material at a constant loading rate of 5 mN/sec under a maximum load of 200 mN.

Two sets of machined wafer edges were analyzed. The first set of wafers was machined with a sharp tip at rake angles of -45° , and depths of cut of 50, 250, and 500 nm. The second set was machined with a rounded diamond tip at rake angles of 0° , -30° , and -45° , and a depth of cut of 300 nm. All of the sample edges were machined at a rate of 20 rev./min. A schematic for the machined SiC wafer edges, and surfaces is shown in Fig. 1. Tool wear can change the sharpness of the tip with use, and therefore, alter the pressures that are achieved at the contact interface of the tool and the material. For the limited machining distances in these experiments, tool wear was not expected to significantly influence the machining results, and was therefore, not considered an issue.

The Raman scattering experiments were performed with two spectrometers, one with macro, and the other with micro focusing optics. In the macro system, a $\sim 45^\circ$

backscattering geometry was employed, and the laser was focused to $\sim 100 \mu\text{m}$ diameter spot on the sample. The Raman experiments were performed with the 244 nm UV line of a frequency doubled argon ion laser (Coherent Inc.), and the scattered light was focused onto the entrance slit of a triple spectrometer (Spex Triple Mate 1877). In the micro Raman system, a 180° backscattering geometry was employed, and the laser was focused to a spot size of $\sim 2 \mu\text{m}$ on the sample. The Raman experiments were also performed with the 244 nm UV line of a frequency doubled Ar ion laser (Lexel Inc.), and the scattered light was focused on the entrance slit of a triple spectrometer (Dilor). For both systems, CCD detection was used to collect the spectra. The probing depth into crystalline 6H-SiC with a 244 nm incident wavelength is $\sim 35 \text{ nm}$ (the values are calculated for the depth in which the intensity of the measured light is 37% of the incident light).

5.3 Results

A. Indented 6H-SiC (0001)

Indentation experiments were performed on a 6H-SiC (0001) wafer to investigate the local bonding properties from controlled point pressure conditions. A SEM image of the indented region is presented in Fig.2. The indented regions indicate an inelastic response with limited macro cracking indicated at the indentation corners. The one-step load displacement curve during indentation is provided in Fig. 3. In Si, a pop-out in the unloading portion of the curve can be produced from a phase transition, which would be accompanied by a volume release or relaxation of densification during unloading. An elbow can indicate the formation of an amorphous phase.¹ The load displacement curve for the SiC indent shows no clear evidence of either a pop-out or an elbow. The load

displacement curves were analyzed for loads ranging from 400 to 10 mN. The curves indicated no clear evidence of a pop-out feature during unloading. However, for the 100 mN load indentation, there may be a small pop-in feature during loading.

Raman spectra were obtained from within the indented plastic zone, and in the surrounding regions. The spectra are given in Fig. 4. Within the indent, the TO, and the LO modes are displaced to higher relative wavenumbers when compared to the reference spectrum, which was obtained far from the indent. The peak displacements indicate compressive stresses. A maximum displacement was observed in the center of the indent. This signifies that the region at the contact point of the diamond tip, and the SiC is the zone of maximum stress. The stress decreases outward from the center. The center peak position of the TO mode is shifted by a larger amount than the center peak position of the LO mode, this may indicate that the material is under biaxial compression.

In addition to the peak displacement, the peaks are broadened. This broadening is attributed to a gradient of residual stresses found within the laser collection volume. A component of the broadening in the TO mode could be due to a range of phonon propagation directions due to the slanted surface, and also due to splitting of the doubly degeneracy of this mode. However, splitting of the mode would require non-uniformity in the plane of the substrate, which may be unlikely for the indents.

Prior diamond anvil cell experiments on 6H-SiC performed by Liu et al. have measured the shift in mode frequency as a function of applied hydrostatic pressure for the TO and

LO modes. The following power law approximations were determined which relate the strain in the crystal to the measured shift in the TO and LO modes:

$$\omega_{E_2}(\sigma) = 789.2 + 3.11\sigma - 0.009\sigma^2 \quad (5.1)$$

$$\omega_{A_1(LO)}(\sigma) = 970.1 + 3.83\sigma - 0.013 \times 10^{-2} \sigma^2 \quad (5.2)$$

where 789.2 Rcm^{-1} and 970.1 Rcm^{-1} are the relaxed values of the TO, and the LO modes respectively, and the stress, σ , is measured in GPa.² We have used these relations to analyze the residual stress in the indentations, and the results are displayed in Fig. 5. In the stress determinations, the center value of the broadened peak was employed, and broadening due to phonon propagation directions, and possible mode splitting were not considered.

B. Machined 6H-SiC (0001) Wafer Edges

Optical microscope inspections of the machined wafer edges indicated areas of ductile, and brittle regions that are dependent of the 6-fold symmetry of the material. Fig. 6 shows a polar plot of the cutting force of the machining tool as a function of crystallographic direction. The relative differences in the forces as a function of crystallographic directions are produced from a higher resistance of the material to deformation and material removal. Regions of higher force indicate ductile machining, and regions of lower force indicate a brittle surface since cracking, and fracture will decrease the cutting forces. A uniform force could indicate a completely ductile or a completely brittle surface.

Optical images of the surfaces indicated that the ductile surface areas were found to increase, and the brittle regions decrease, for both a larger range of crystalline directions, in addition to fracture decrease within the ductile regions, with smaller depths of cut, and higher negative rake angles. When machining with a -45° rake angle sharp tip, a 50 nm depth of cut the machined wafer edges were almost completely ductile, while for a 500 nm depth of cut were found to be almost completely brittle. Furthermore, the rake angle directly influenced the ductile, and brittle regions. A larger surface area of ductile response can be produced with a larger negative rake angle. At a machining depth of 300 nm with a rounded tip, a -45° rake angle produced mostly ductile surfaces, and a 0° rake angle produced mostly brittle surfaces.

The material removed during the machining process also indicated a ductile response. Fig. 7 shows an optical image of a ductile chip removed during the machining process indicated by the elongated nature, and limited fracture. The chips produced from the ductile machining parameters produce elongated chips, while the chips removed from a brittle machining process were fractured. The relative percentages of ductile chips to brittle chips removed during machining were found to increase for shallower depths of cut, and larger negative rake angles.

Raman scattering of a machined wafer edge of 6H-SiC were acquired along the $[11\bar{2}0]$ direction (*i.e.* corresponding to a larger force direction as indicated in Fig. 6) is shown in Fig. 8. A micro Raman scattering spectrum of a non-machined 6H-SiC wafer edge in the $[11\bar{2}0]$ wafer direction, and the calculated phonon density of states for SiC are shown for

comparison. The spectrum of the machined edge display broadened peaks. The TO mode center frequency is displaced to a higher relative wavenumber while the LO mode center frequency is displaced to a lower relative wavenumber from their crystalline peaks. The broadened displaced TO peak may be attributed to randomly oriented polycrystalline material since the TO mode frequency shifts in this direction for different phonon propagation directions.³ Because of the width of the features, the presence of residual stress cannot be excluded. The TO and LO mode splitting is derived from both the anisotropy of the material, and an electrostatic component of the Si and C atoms. A decrease in the TO-LO splitting may indicate small grain size polycrystalline material which would decrease the long range electrostatic component resulting in an overall decrease in the component of the splitting that is attributed to the electrostatic interaction. In the limit, where the domain size decreases to zero, and the structure resembles a random network, the material is amorphous, all of the Raman modes become active, and the spectrum is expected to resemble the density of states.

The crystal structure of the wafer edges were analyzed after machining with a spherical tip at rake angles 0, -35° , and -45° . The machining depth of cut was 300 nm for each revolution. The spectra are presented in Fig. 9. The results indicate that the full width at half maximum (FWHM) of the TO mode decreases as the negative rake angle is decreased. This indicates a polycrystalline surface layer that may be more disordered or thicker for larger negative rake angles.

The crystal structures of the machined edges were analyzed for a depth of cut of 50, 250, and 500 nm. The surfaces were machined with a sharp tip, and a rake angle of -45° . Raman scattering measurements were obtained from a region of the sample corresponding to the $[11\bar{2}0]$ direction (see Fig. 6). Fig. 10 indicates that the FWHM for the TO and LO modes is larger for cuts of 50 and 250 nm and decreases when the cut is 500 nm in depth. This indicates a polycrystalline surface layer that may be more disordered or thicker for shallower depths of cut.

As an interesting side note, localized dark spots were observed on the surface of the machined wafer edges. The Raman spectrum from these regions is shown in Fig. 11. The double peak feature is characteristic of sp^2 graphitic type C-C bonding. It is possible that the bonding originated from segregation of C from the SiC bulk on the machined surface. Visible Raman spectra of the bulk do not show sp^2 graphitic type inclusions indicating that the bonding is limited to the surface. We also considered whether the dark spots could be residue left from the diamond tip. However, Raman analysis of machined Si surfaces does not show evidence of sp^2 -bonded carbon suggesting that the tip is not responsible for the affect.

5.4 Discussion

We consider first the evidence of phase transformation in the indented regions. The SEM image of the indentation indicates severe plastic deformation of the 6H-SiC with limited cracking, and the displaced material seems to have a ductile response. However, the load displacement curve, and Raman spectra do not show clear evidence of a phase change or

residual phases. The unloading portion of the load displacement curve does not indicate a pop-out, and the Raman scattering spectrum does not indicate residual metastable phases or polytype transformation. The Raman spectra indicated that the plastic zone of the indentation, although stressed, has a crystalline form. The residual stresses indicate 6H-SiC lattice has not relaxed.

The difference in stress measurements for the TO and LO modes suggests biaxial stress. A larger residual stress is found in the direction perpendicular to the c -axis even though force was applied parallel to the c -axis. This could indicate that the elasticity of the material in the direction parallel to the c -axis is greater than perpendicular to the c -axis, and hence, the material can recover to a greater extent in this direction. The broadening in the TO peak can be attributed to a distribution of atomic stresses perpendicular to the c -axis within the laser collection volume. A component of this broadening could also be due to a range of phonon propagation directions on the indented surface.

The machining results also indicate ductile plastic flow of the machined surface. The Raman spectra indicated a residual polycrystalline phase on the ductile surfaces. Raman scattering measurements were acquired for the $[11\bar{2}0]$ crystallographic wafer direction. This direction has been found most likely to produce a ductile response (*i.e.* a high cutting force direction on the polar plot of Fig. 6). A polycrystalline structure for shallower depths of cut, and larger negative rake angles is indicated. A polycrystalline surface layer for shallower depths of cut could be due to a larger amount of material machined away as debris with larger depths of cut. Furthermore, a polycrystalline

surface layer for larger negative rake angles could be due to a larger degree of compressive stresses generated with larger negative rake angles, or a larger extent of the high pressure phases produced during the machining process. Results have indicated that a larger negative rake angle will create higher compressive stresses at the machining contact interface.⁴ Thus, a larger extent of the transformed region could be expected for larger negative rake angles.

5.5 Concluding Remarks

UV Raman spectroscopy has allowed for investigation of the surface of indented 6H-SiC (0001), and machined 6H-SiC (0001) wafer edges. The measurements are obtained for probing depths within 35 nm of the materials surface with the 244 nm UV wavelength.

It was found that indentation of 6H-SiC (0001) surfaces produces an inelastic response, and that macro cracking decreases with a decrease in load. UV Raman scattering measurements of a 200 mN load indentation indicate residual biaxial compressive stresses. Stress, and stress gradient are found to be greatest in the center of the indent, and in a direction perpendicular to the c-axis.

The machined wafer edges also indicated a ductile response. It was found that the surface area of a ductile response on the wafer edges increases with shallower depths of cut, and larger negative rake angles. Furthermore, the relative percentage of ductile material removal to brittle material removal is found to also increase with shallower depths of cut, and larger negative rake angles, which is probably a direct consequence of

the increased ductile surface areas on the wafer edges. The increase in ductile surface area for a larger range of crystallographic directions can be explained by the stresses generated during the machining process that are dependent on the symmetry of the crystal and can relax or prevent formation of the high-pressure metallic phase and residual structures. For a given crystallographic wafer direction, the higher extent of a ductile response for shallower depths of cut and larger negative rake angles can be explained with larger amount of material removal of the transformed zone with larger depths of cut, and a higher extent of the transformed regions created with larger negative rake angles. The structural changes on the ductile surfaces suggest that transition to a metallic phase in 6H-SiC could allow precision machining of these materials.

5.6 References

1. V. Domnich, Y. Gogotsi, S. Dub, *Appl. Phys. Lett.* 76, 16 2214 (2000).
2. J. Liu, Y. K. Vohra, *Phys. Rev. Lett.* 72, (26) 4105 (1994).
3. D.W. Feldman, J.H. Parker, JR., W.J. Choyke, Lyle Patrick, *Phys. Rev.* 173, 787 (1968).
4. T.G. Kumbera, H.P. Cherukuri, J.A. Patten, C.J. Brand, T. D. Marusich, *Machining Science and Technology* 5, 3 341 (2001).

(a)

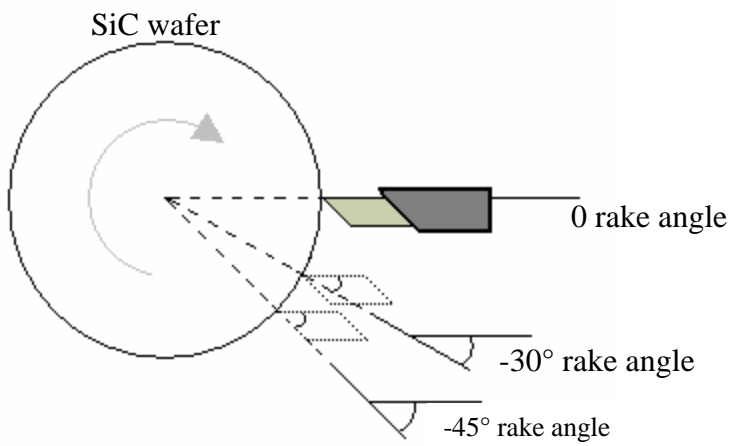


FIG 1: Schematic of the machining process of 6H-SiC (0001) wafer.

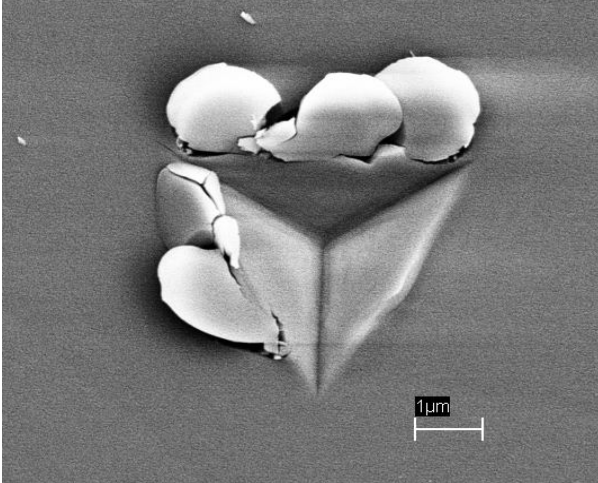


FIG 2: An SEM image of the surface of indented 6H-SiC. A maximum load of 200 mN was used.

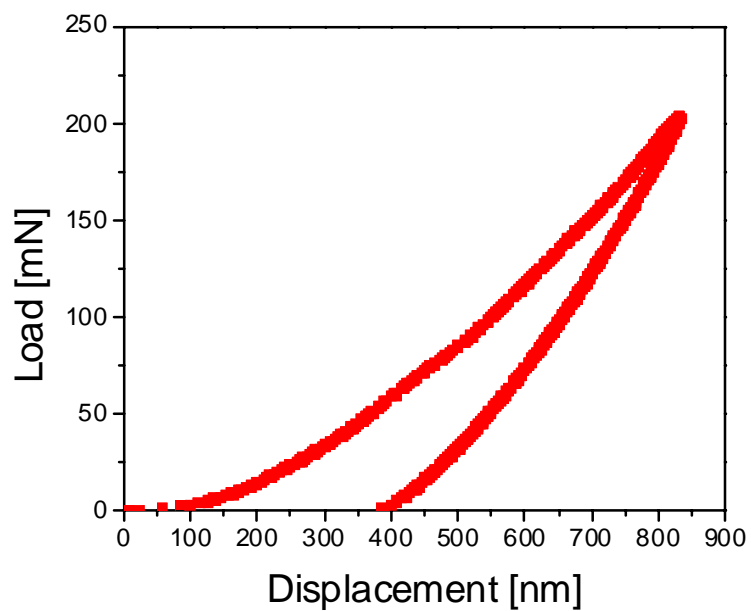


FIG 3: The load displacement curve for indentation of a 6H-SiC(0001) surface with a maximum load of 200 mN.

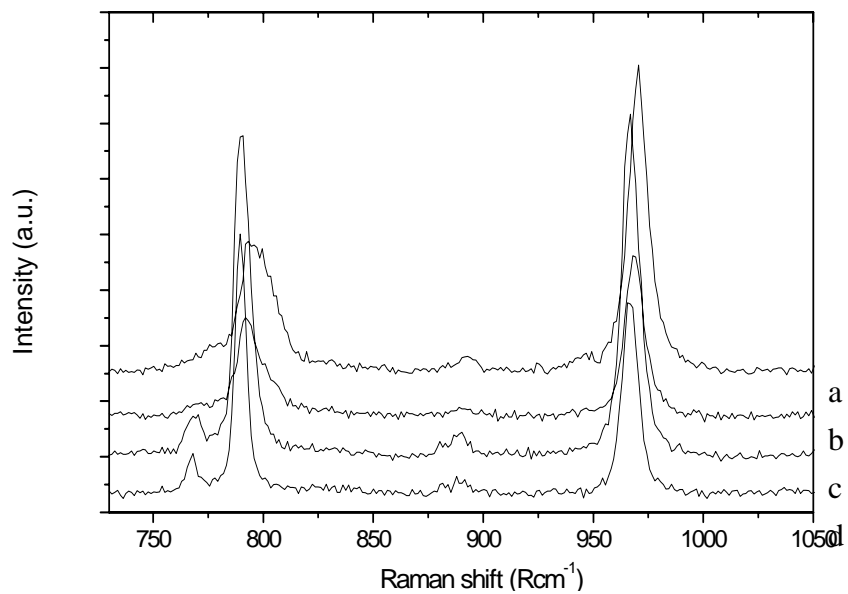


FIG 4: UV micro Raman scattering spectra display the TO, and LO modes for (a) center of the indent (b) edge of the indent (c) surrounding area (d) reference area for indentation with a maximum load of 200 mN.

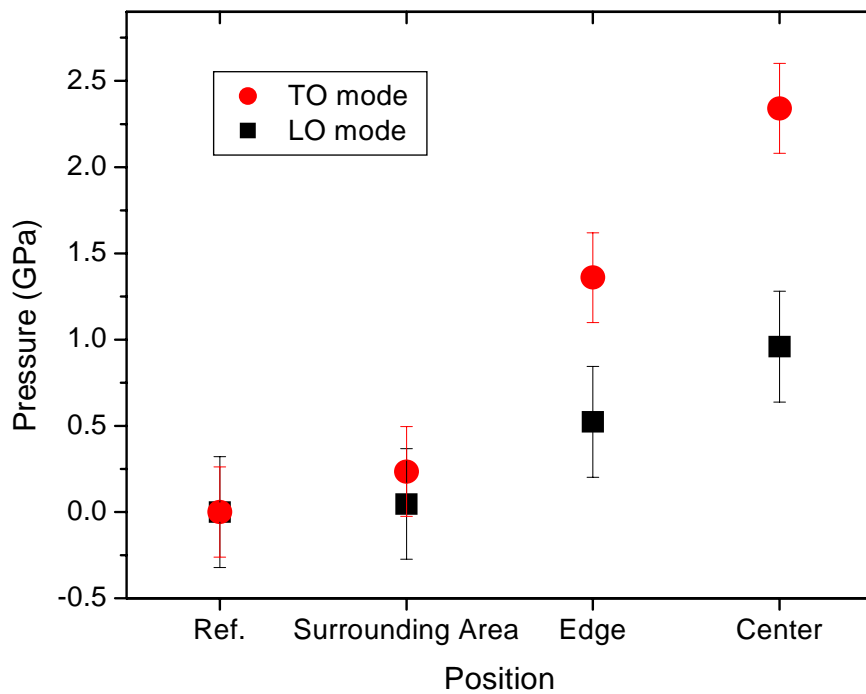


FIG 5: The local stress (in units of pressure) in regions in, and surrounding an indent. The values were deduced from the transverse (TO), and longitudinal (LO) Raman scattering modes. The results were obtained from indents produced from a maximum indentation load of 200mN, and the stress was deduced using the relations from Liu, et al.²

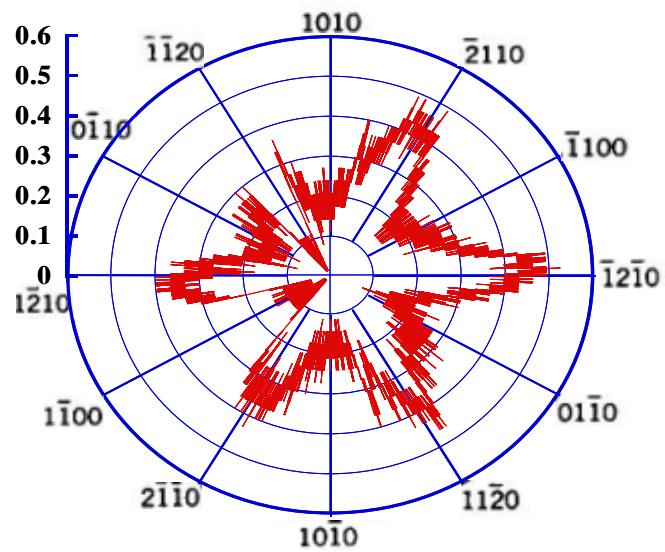


FIG 6: Polar plot of the cutting force dependence on the 6-fold symmetry of 6H-SiC machined wafer edges. The plot was obtained for a rake angle of 0° , and a cutting depth of 100 nm.

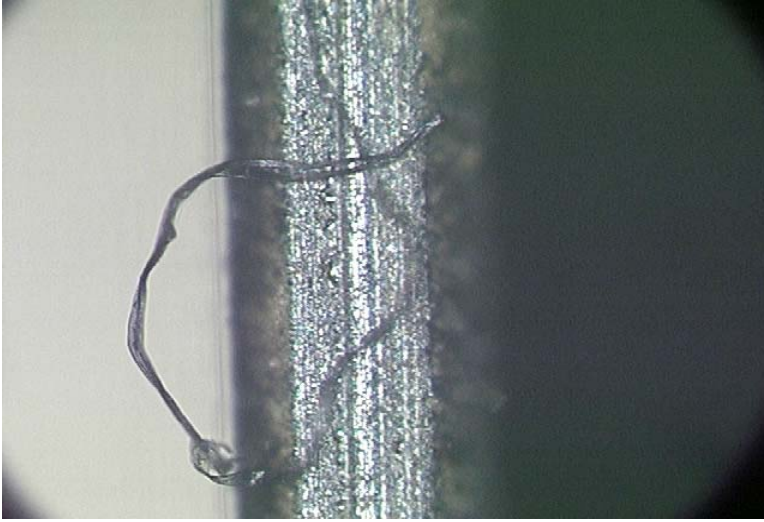


FIG 7: Optical image of ductile chip removal. A rake angle of -45° , and a depth of cut of 500 nm were employed.

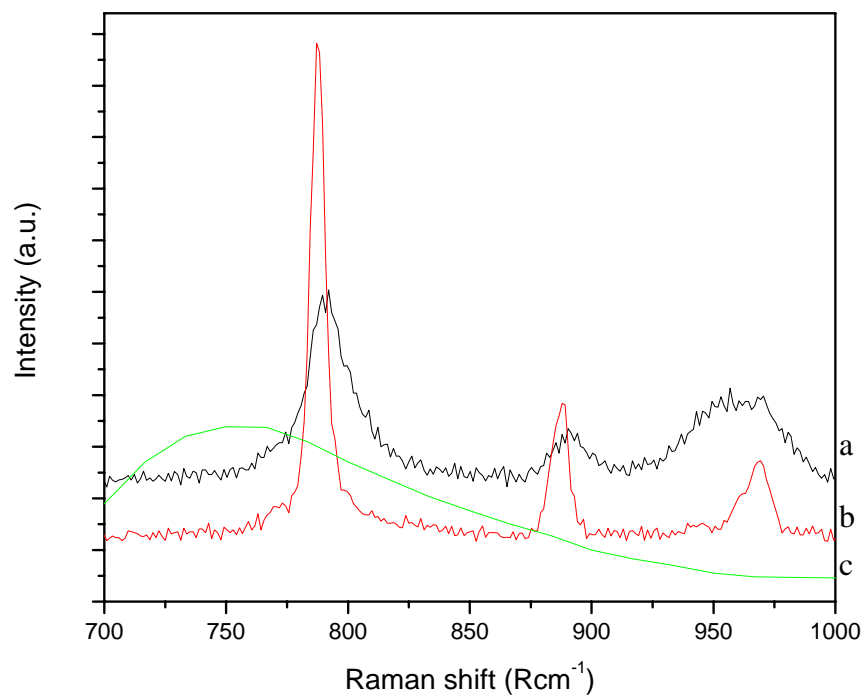


FIG 8: UV micro Raman scattering spectra of (a) machined ductile 6H-SiC edge, and a (b) non-machined 6H-SiC wafer edge. For comparison, the (c) calculated vibrational density of states (DOS) of SiC is presented.

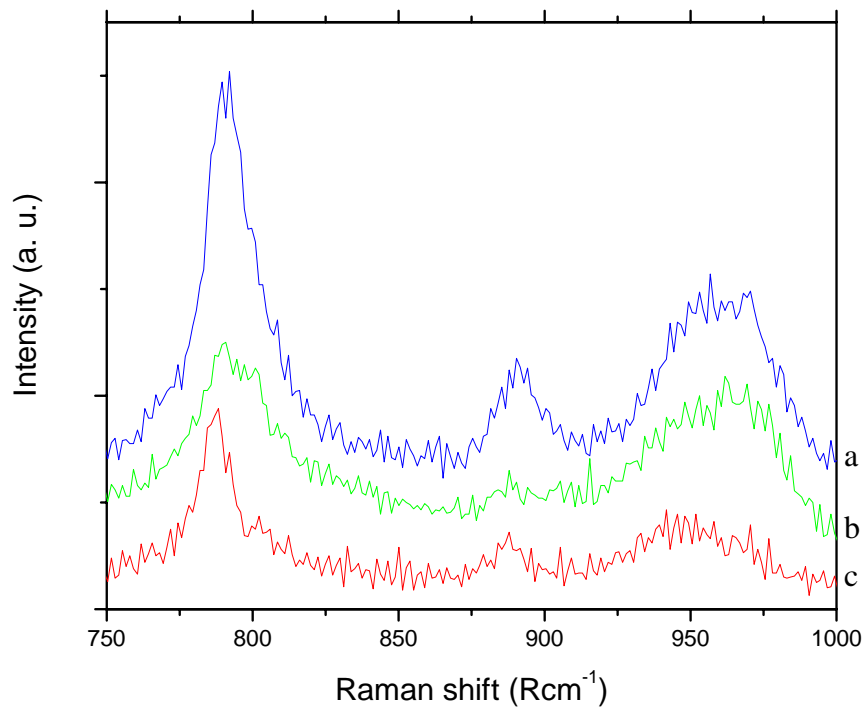


FIG 9: UV micro Raman scattering spectra of machined 6H-SiC edges for rake angles of (a) -45° , (b) -30° , and (c) 0° . The spectra were obtained with incident light along the $[11\bar{2}0]$ direction of the wafer.

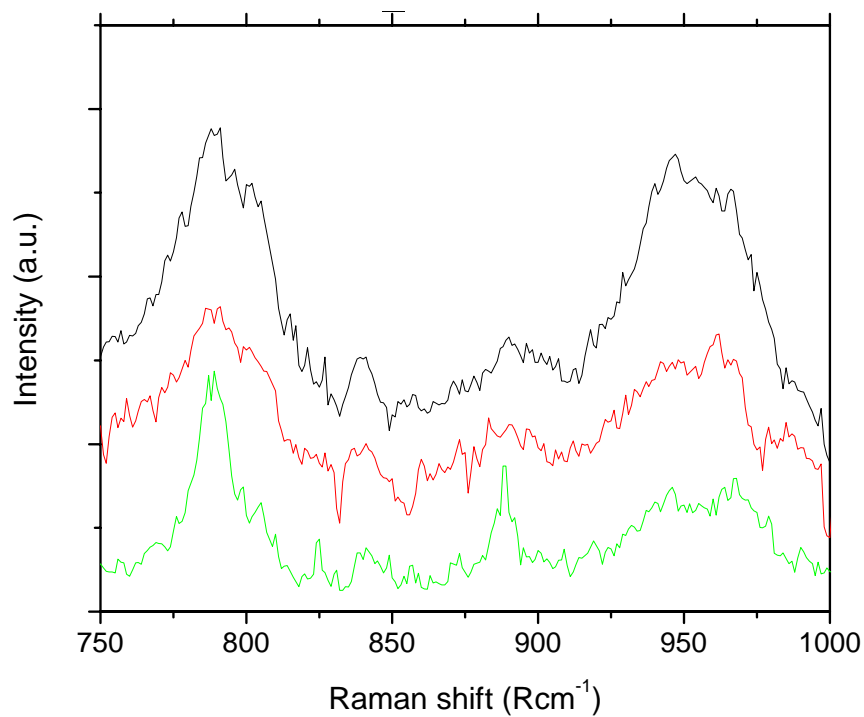


FIG 10: UV macro Raman scattering spectra of machined 6H-SiC edges for machining depths of (a) 50, (b) 250, and (c) 500 nm depth of cut per revolution. The spectra were obtained with the incident light along the $[11\bar{2}0]$ direction of the wafer.

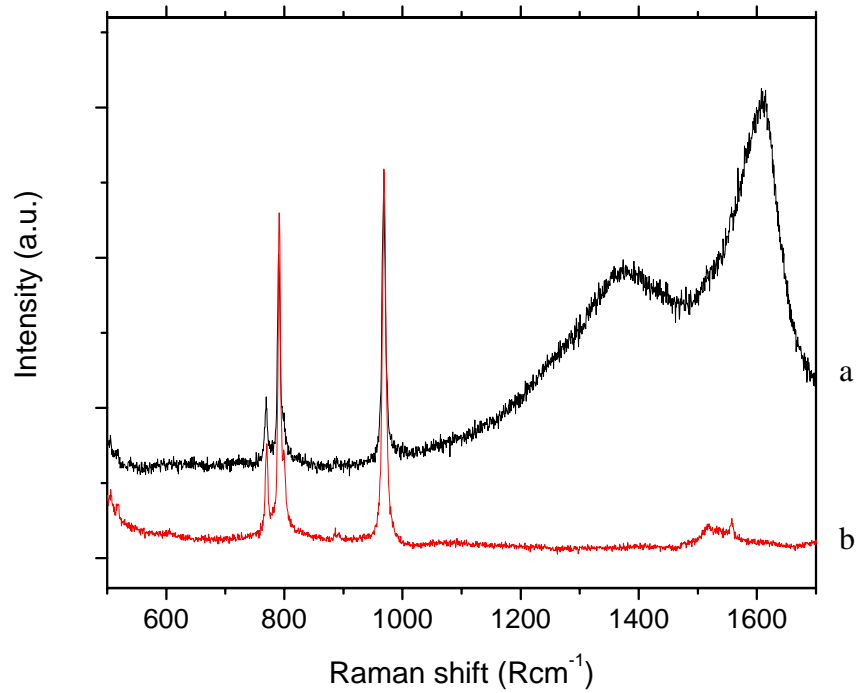


FIG 11: UV micro Raman scattering spectra of a (a) dark spot on the machined surface (b) compared to the machined surface of a 6H SiC wafer.

6. UV Raman Scattering Analysis of Machined β -Si₃N₄

Jennifer J.H. Walter¹, Mengning Liang¹, Xiang-Bai Chen², Leah Bergman², John A. Patten³, Robert J. Nemanich¹

¹*North Carolina State University, Raleigh, NC 27695*

²*University of Idaho, Moscow, ID 83843*

³*University of Western Michigan, Kalamazoo, MI 49008-5314*

6.1. Experimental Summary

This study addresses the properties of precision-machined polycrystalline β -Si₃N₄ surfaces. Prior research has reported ductile surface properties produced from indentation and grinding of β -Si₃N₄.^{1, 2} It is possible that the pressure-induced plasticity is similar to that found in Si with its origin in a high pressure phase transformation to a metallic phase. Preliminary diamond anvil cell experiments of β -Si₃N₄ indicate low-energy X-ray diffraction peaks at pressures between 20 and 35 GPa suggesting an unidentified high-pressure phase.⁵ Raman scattering of the ductile surfaces indicate a residual layer of an amorphous phase. This amorphous surface layer may be the relaxed phase of a high-pressure metallic phase. We have used wavelength dependence Raman spectroscopy to probe the depth dependence of the residual amorphous zone left from machining. The short absorption depth of UV light allows for accurate probing of the surface, and the transparency to visible light allows for analysis of the bulk material.

6.2 Experimental Details

The β -Si₃N₄ surfaces were prepared first by grinding and then machining over the ground surface. The machining was employed for depths of cut of 500 nm, 5 μ m, and 10 μ m. Si inclusions in the bulk material were deduced from the visible Raman spectra, which

showed a peak at 520 Rcm^{-1} . Because of the slow machining speeds employed, we expect that there was a minimal increase in temperature. Tool wear could influence the analysis by changing the sharpness of the tip with use. However, for the limited machining distances in these tests we expect that wear was not an issue.

The Raman scattering experiments were performed with two spectrometers, one with macro and the other with micro focusing optics. In the macro system, a $\sim 45^\circ$ backscattering geometry was employed and the laser was focused to $100 \mu\text{m}$ spot on the sample. The Raman experiments were performed with the 244 nm UV line of a frequency doubled argon ion laser (Coherent Inc.), and the scattered light was focused onto the entrance slit of a triple spectrometer (Spex Triple Mate 1877). In the micro Raman system, a 180° backscattering geometry was employed and the laser light was focused to a spot size of $\sim 2 \mu\text{m}$ on the sample. The Raman experiments were performed with the 244 nm UV line of a frequency doubled Ar ion laser (Lexel Inc.) and the 325 nm UV line wavelength of a HeCd ion laser (Kimmon Electric Inc.), and the scattered light was focused onto the entrance slit of a triple spectrometer (Dilor). For both systems, CCD detection was used to collect the spectra. The probing depth into polycrystalline $\beta\text{-Si}_3\text{N}_4$ with a 244 nm line is $\sim 1.4 \mu\text{m}$ (the values are calculated for the depth in which the intensity of the light is 37% of the incident intensity).

6.3 Results

A SEM image of a chip removed from the surface during machining is presented in Fig.

1. The chips shown are of the order of a μm thick. The image indicates that the material

was bent and distorted without fracture indicating that the material removed from the surface is ductile.

The spectra presented in Fig. 2 represent data collected with an excitation wavelength of 244 nm and were obtained from the surface of machined β -Si₃N₄, at depths of cut of 500 nm, 5 μ m, and 10 μ m. The Raman scattering spectra of the machined surfaces show broad features, and the sharp peaks associated with crystalline structures are absent. This broadening can be related to the broadened phonon density of states representing an amorphous structure. The broadened density of states contains two broadened peaks centered at \sim 400 and \sim 900 Rcm⁻¹.⁶ In comparison, the ground surfaces exhibit crystalline peaks with some evidence of an amorphous component.

Fig. 3 presents the Raman scattering spectra of the machined β -Si₃N₄ surface for a 5 μ m depth of cut and incident wavelengths of 514.5, 325, and 244 nm. The 514.5 nm visible Raman scattering spectrum indicates sharp crystalline peaks. In the spectrum obtained with the 325 nm incident wavelength, the peaks are slightly broader, but the broad background. The spectrum obtained with the 244 nm incident wavelength indicates a completely broadened spectrum. The results indicate that the bulk of the material is crystalline indicated by the sharp peaks and the surface is amorphous indicated by the broadening.

The Raman scattering spectrum of the chips removed from the surface is shown in Fig. 4. The broadened peaks indicated in the micro and macro Raman scattering spectra indicate

that the chips are amorphous. There is some extent of crystalline peaks observed in the micro Raman scattering spectrum indicating that the power density produced by the small spot size in micro Raman scattering spectrum was high enough to heat and crystallize the chips.

6.4 Discussion

Machining for depths of cut on the nm and μm scale resulted in a ductile surface and ductile material removal. Raman scattering measurements of the ductile, machined surfaces indicated an amorphous layer. The spectra from the grounded regions indicated crystalline peaks, with some amorphous component. It is possible that the amorphous remnants result from surface polishing of the material before grinding or that these amorphous remnants are a direct result of the grinding. The sharp peaks in the visible Raman spectra of the machined surfaces indicate that the bulk of the material is crystalline, and the broadened peaks in the UV spectra indicate that the surface is amorphous. The Raman scattering spectra of the debris removed from the surface during machining indicate that the chips are also amorphous. Although it has been demonstrated that while machining a higher degree of compressive stresses while machining are generated within the chip,⁷ it is expected that the material removed from the surface should have a similar structure of the surface.

A direct crystalline to amorphous transformation is not expected at room temperatures. Therefore, the amorphous layer may result from relaxation from a high-pressure metallic phase and the metallic phase may be responsible for the ductile behavior.

6.5 Conclusions

It has been found that β -Si₃N₄ can be machined in a ductile regime for cutting depths on a scale of μm and nm , and is evidenced by a smooth surface finish and ductile chips removed during machining. The machined surfaces indicated a residual amorphous layer where the extent of the amorphous layer is limited to the materials surface. The residual amorphous phase may result from relaxation of a high-pressure metallic phase. X-ray diffraction peaks indicate a high-pressure phase at ambient temperature. The high-pressure metallic phase could explain the origin of the ductile response observed on the surface of this brittle material.

6.6 References

1. J. Patten, *Advances in Abrasive Technology III (Japan Society of Abrasive Technology, Tokyo, 2000)* p. 87.
2. C. Ullner, J. Beckmann, and R. Morrell, *J. Eur. Ceram. Soc.* 22, 1183 (2002).
3. J.J. Gilman, *Philos. Mag. B* 67, 207 (1993).
4. V. Domnich, Y. Gogotsi, *Experimental methods in the physical science* 38, 355 (2001).
5. C. Ullner, J. Beckmann, and R. Morrell, *J. Eur. Ceram. Soc.* 22, 1183 (2002).
6. N. Wafa, S.A. Solin, J. Wong, and S. Prochazka, *J. Non-Crys. Solids* 43, 7 (1981).
7. J. Morris, D. Callahan, J. Kulik, J. Patten, and R. Scattergood, *J. Am. Ceram. Soc.* 78, 2015 (1995).

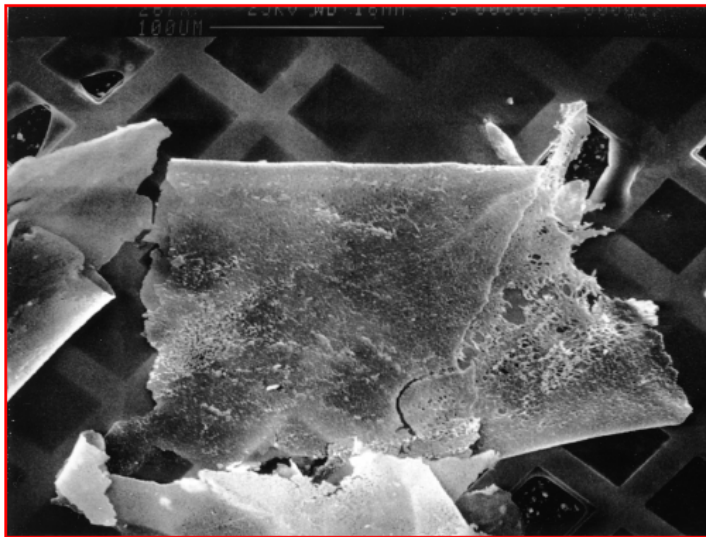


FIG 1: SEM image (400 μm x 400 μm) of debris from machined β - Si_3N_4 .

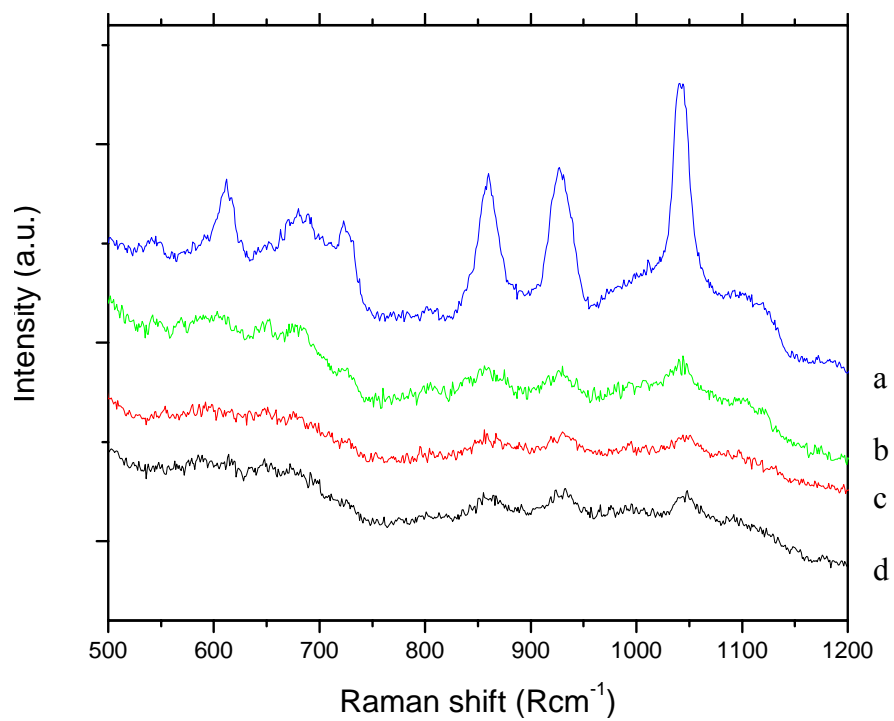


FIG 2: UV Raman scattering spectra of (a) grounded and machined (b) 5 μm (c) 10 μm and (d) 500 nm polycrystalline $\beta\text{-Si}_3\text{N}_4$.

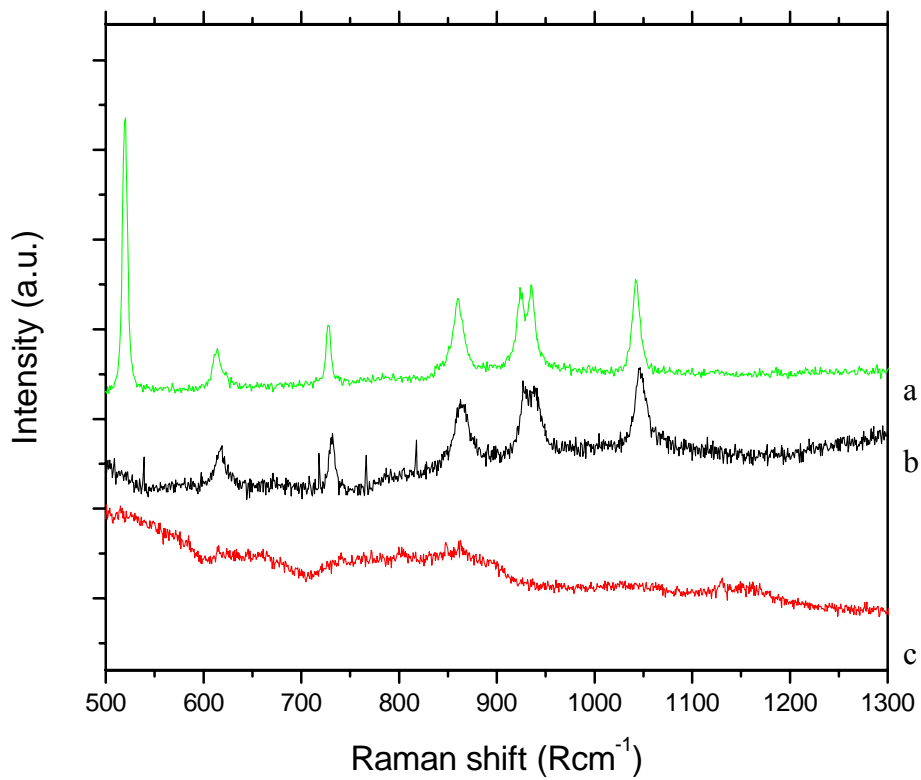


FIG 3: (a) Macro Raman scattering spectrum of the bulk of machined β -Si₃N₄ is shown for 514.5 nm. Micro Raman scattering spectra with (b) 325 and (c) 244 nm incident wavelengths.

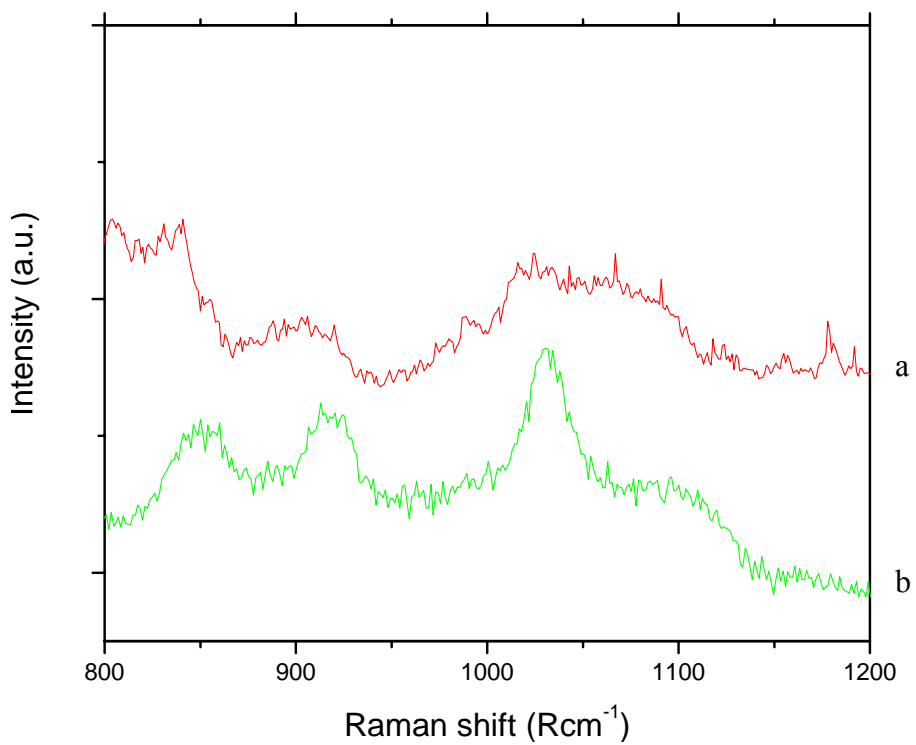


FIG 4: (a) Macro and (b) micro Raman scattering spectrum of the chips removed during the machining process for a 5 μm depth of cut.

7. Concluding Remarks and Future Directions

It has been found that Si, 6H-SiC, and β -Si₃N₄ can be machined in the ductile regime for cutting depths from the μm to the nm scales. The residual phases, and the ductility of the materials studied have been found to have direct dependences on the scale of the cutting depth, the rake angle tool geometry, and the crystallographic direction of the material relative to the cutting direction. A transition path involving densification from covalent bonding to metallic bonding during compression at the contact interface of the machining tool and the material could describe the observed ductile plastic flow. Upon pressure release, the metallic phase can then relax to metastable phases or to a different structure. In fact, the ductile surfaces measured in this study indicate such residual phases. We have employed Raman spectroscopy to investigate the bonding structures of the residual phases. Using visible and UV wavelengths the surface plastic zone of deformation has been obtained for the materials studied. This technique has proven to be a powerful and nondestructive tool.

Controlled point pressure experiments of low load Si indents indicate local residual metastable and amorphous phases that have been previously identified in diamond anvil cell experiments as decompression phases from the metallic phase. For higher load indents, Si will experience brittle fracture. In addition, controlled point pressures of 6H-SiC indicate a ductile surfaces and residual stresses within the indentation.

The Si ductile-machined surfaces indicate an amorphous surface layer. The extent of the amorphous layer has been found to be greater when machining at a lower material removal rate (*i.e.* at smaller lateral distances of travel per each revolution during machining). It has also been found that the ceramic materials, 6H-SiC and β -Si₃N₄, can be machined in the ductile regime. Machining of 6H-SiC (0001) wafer edges results in a residual polycrystalline structure. The extent of the polycrystalline layer has been determined to increase for shallower machining depths of cut. Moreover, machining of β -Si₃N₄ on the nm and μ m scale also results in the formation of a surface layer of residual amorphous material. At larger material removal rates, more material is machined away as debris, which could explain the thinning amorphous layer.

The tool rake angle can also have an affect the resulting ductility and residual phases in these materials. Machined 6H-SiC indicated a residual ductile surface for larger negative rake angles. The extent of the residual polycrystalline phase was found to increase with increased negative rake angles. It has been suggested that an increased negative rake angle will generate a larger degree of pressure between the machining tool and the material, which could explain the transformation dependence on machining rake angle. Therefore, the geometry of the machining tool with respect to the material surface can also effect the stress field causing different responses of the material.

The ductile regions of the Si surfaces, and 6H-SiC machined wafer edges, are found to have a crystallographic dependence. At larger cutting depths, fracture and shear stresses

become dominate. The surface areas of ductile regions are found to decrease, while the surface area of brittle regions increase.

The metastable residual structures are typically higher energy states than the parent structure at ambient temperature. It is therefore unlikely for a direct transformation between the parent structures to the metastable phases. Thus, the presence of the residual phases provides evidence of compression and relaxation from a high-pressure metallic phase. However, other mechanisms than the described transition path should be considered as the origin of the ductile surfaces and residual phases. For example, it has been suggested that propagation of dislocations during machining can result in a transformed surface structure, which could resemble a polycrystalline or amorphous phase.

Although significant progress has been made in the characterization of the plasticity of these materials, further *in-situ* analysis of material lattice deformation merits closer attention. This knowledge would not only aid in increasing the efficacy of machining processes by controlling material ductility, but also add to our understanding of the stability of the many different phases, structures, and polytypes and the mechanism of transformation between them.